AGRICULTURE

Spatially differential regulation of ATF2 phosphorylation contributes to warning coloration of gregarious locusts

Xinle Kang[1]†, Meiling Yang[2]†, Xiaoshuang Cui[3], Huimin Wang[2], Le Kang[1,3]*

Warning coloration are common defense strategies used by animals to deter predators. Pestilential gregarious locusts exhibit a notable black-brown pattern as a form of warning coloration. However, the mechanisms regulating this distinctive pattern remain largely unknown. Here, we revealed that the black and brown integuments of locusts are governed by varying amounts of β-carotene and β-carotene–binding protein (βCBP) complexes. β*CBP* expression is regulated by the bZIP transcription factor activation transcription factor 2 (ATF2), which is activated by protein kinase C alpha in response to crowding. Specifically, ATF2 is phosphorylated at Ser^{327} and translocates to the nucleus, where it binds to the β*CBP* promoter and stimulates overexpression. Differential phosphorylation of ATF2 leads to the divergent black and brown coloration in gregarious locusts. The accumulation of red pigments vital for creating the brown sternum depends on βCBP overexpression. The spatial variation in ATF2 phosphorylation enables locusts to rapidly adapt to changing environment for aposematism.

INTRODUCTION

Aposematism coloration is a widely used defense strategy in both terrestrial and aquatic animals. This distinct coloration facilitates adaptation and survival in the presence of predation risks by serving as a warning signal to predators. As a result, predators are triggered to avoid prey that displays conspicuous coloration (*1*, *2*). Environmental signals, particularly related to changes in background cues and predator guilds, can influence the use of high-contrast coloration for defense (*3*). In addition, the density of individuals in a population can cause animals to display conspicuous or cryptic coloration alternatively. Understanding the mechanisms underlying these differences is crucial for animals to adopt the most effective defense strategy against predation. One notable challenge in the evolution of aposematism is determining how conspicuous coloration is rapidly formed while animals are living in swarms.

Aposematism acts by linking conspicuous coloration with the existence of defenses, such as toxins or unpalatability (*4*). Insects use contrasting hues as warning colors, such as black-yellow, black-red, black-brown (orange), and others. Locusts exhibit some of the most notable phenotypic color changes between solitary and gregarious phases to adapt to different population densities (*5*). At high population densities, billions of locusts form immense swarms, which naturally expose them to predators. Consequently, the migratory locust, *Locusta migratoria* (Orthoptera: Acrididae), within the swarms develop a sharp contrast pattern of a black tergum and a brown sternum. In contrast, conspecific solitary locusts living in low density tend to have cryptic green coloration that aids them in blending with their surroundings and avoiding predators (*6*–*8*). The body coloration of gregarious locusts serves in collective behavior, thermal regulation, and alerting against natural enemies (*7*, *9*, *10*). The warning color alone is often not enough to protect insects from predators in nature, although birds tend to prey on green solitary locusts rather than dark-brown gregarious ones (*10*). In addition to warning coloration, gregarious migratory locusts also use phenylacetonitrile (PAN) as an olfactory aposematic signal and toxin precursor for hydrogen cyanide (HCN). When disturbed or preyed upon by birds, the PAN in the locusts is immediately converted to HCN (*10*). The distinctive body coloration of gregarious locusts is strongly linked to their olfactory aposematic signal and HCN toxin (*11*). Similarly, the aposematism of the monarch butterfly (*Danaus plexippus*) is characterized by a unique pattern of black and orange colors that functions as a warning to predators of its toxicity (*12*). Thus, studies on warning coloration and the regulatory mechanism of locusts are crucial in both the fields of biology and pest control.

Numerous approaches have examined the development of locust body color including physiology, genes, and regulatory molecules. A previous study suggested that juvenile hormone is involved in green coloration in solitary locusts (*13*). Recent research indicated that the black coloration on the dorsal region of gregarious locusts is not due to melanin pigmentation but is instead the result of the superposition effect of the β-carotene–binding protein (βCBP)–β-carotene complex–mediated red coloration on the green-colored background that is present in solitary locusts (*14*). Moreover, the divergent body color pattern on gregarious locusts is expressed as a stable phenotype characterized by black-brown coloration (*14*). While pigment effector genes are influenced by transcription factors (TFs) and patterning genes in butterflies and beetles (*15*–*18*), the precise regulatory mechanism governing the contrasting color patterns observed on the tergum and sternum of migratory locusts remains unclear.

Here, we systematically investigated the pigments and pigment binding proteins present in the gregarious black tergum and brown sternum of migratory locusts. Our findings indicate that

[1]Beijing Institutes of Life Science, Chinese Academy of Sciences, Beijing 100101, China. [2]College of Life Science, Capital Normal University, Beijing 100048, China. [3]State Key Laboratory of Integrated Management of Pest Insects and Rodents, Institute of Zoology, Chinese Academy of Sciences, Beijing 100101, China.
*Corresponding author. Email: lkang@ioz.ac.cn
†These authors contributed equally to this work.

differential levels of βCBP play a crucial role in controlling the black-brown coloration of gregarious locusts. This regulation mechanism occurs through the activation of transcription factor 2 (ATF2) phosphorylation in various parts of the integument. Specifically, the level of ATF2 phosphorylation determines the level of β*CBP* transcription, which further regulates the warning coloration in locusts in response to changes in population density. Our study provides crucial insights into the precise coordination of warning coloration in gregarious locusts, facilitating their collective defense against predators.

RESULTS

Black-brown coloration of gregarious locusts depends on the distribution of the βCBP–β-carotene complex

Gregarious locusts display a distinct coloration pattern, with a black back and brown venter on the thorax and abdomen (Fig. 1A). To elucidate the mechanisms responsible for the contrast in body coloration between the black and brown integuments, we conducted a quantitative proteomic analysis. We extracted proteins from the thorax and abdomen integuments of gregarious locusts with the aforementioned colors and identified 1006 corresponding peptides, of which we could quantify 772 proteins (table S1). Comparative analysis revealed 170 up-regulated differentially expressed proteins (DEPs) in the brown integuments, while 52 up-regulated DEPs in the black integuments (Fig. 1B). Among the quantified proteins, 34 were found to be involved in pathways associated with animal coloration (fig. S1). Notably, 11 DEPs exhibited high expression in the brown integuments and 5 DEPs displayed high expression in the black integuments among these 34 proteins (Fig. 1C). The differential expression of βCBPs in the black and brown integuments of gregarious locusts was investigated due to its role in locust coloration (*14*). Three βCBPs (LOCMI13402, LOCMI17258, and LOCMI14013) displayed distinct expression patterns, in which LOCMI13402 exhibited higher expression in the brown integuments, while LOCMI17258 and LOCMI14013 were up-regulated in the black integuments (Fig. 1C). Knockdown experiments demonstrated that *LOCMI13402* is involved in regulating the black and brown coloration of the pronotum and prosternum (fig. S2, A and B). Therefore, further investigation focused on the LOCMI13402 βCBP. In addition, polymerase chain reaction (PCR) amplification was conducted to assess the expression levels of this β*CBP* between the black tergum and brown sternum. Compared to solitary locusts, higher levels of β*CBP* were detected in the integument of gregarious locusts. In addition, the level of β*CBP* was higher in the brown sternum than in the black tergum of the thorax and abdomen (Fig. 1D). We then detected β-carotene levels bound with βCBP protein in different parts of the body based on the body coloration that emerged from the combination of β-carotene and βCBP protein complex (fig. S3) (*19*). We found that the β-carotene content in the prosternum (24.28 μg/g) was twice as high as that in the pronotum (11.13 μg/g), and in the abdomen, the β-carotene content in the sternum (18.24 μg/g) was significantly higher than that in the tergum (9.86 μg/g) (Fig. 1E). Moreover, colloidal gold immunoelectron microscopy showed that more βCBP-conjugated gold particles accumulated in the pigment granules of the prosternum than in those of the pronotum (Fig. 1, F and G). Because the trend of β*CBP* expression and β-carotene content in the tergum and sternum was consistent across the thorax and abdomen, subsequent experiments focused on the pronotum and prosternum as they can effectively reflect the regularity of body color changes.

The electroporation-mediated RNA interference (RNAi) experiments conducted in the locust epidermis demonstrated that β*CBP* knockdown specifically eliminate β*CBP* expression and pigment coloring without any change in the cuticle morphological characteristics in the RNAi-treated region of the prosternum compared to those in the negative control region (fig. S2, C and D). Thus, the body color pattern of the black pronotum and the brown prosternum in gregarious locusts is closely related to differences in βCBP expression and β-carotene content, as well as to the content of the βCBP–β-carotene complex.

ATF2 is a TF for β*CBP*

As potential TFs may be regulated β*CBP* levels in different parts of the integument (*15*–*18*) by binding to target gene promoters, we conducted an investigation to identify the putative promoter of β*CBP*. We carried out genome walking using the locust's whole-genome sequences (*20*) to confirm a ~1.2-kb genomic region positioned upstream of the β*CBP* coding sequence. To assess promoter activity, we used dual luciferase reporter plasmid assays with different regions of the promoter. Among the tested regions, the −184– to +1–base pair (bp) region exhibited the highest expression when compared to the reference reporter. This suggests that the core promoter region of β*CBP* is located between −184 and −102 bp (Fig. 2A).

The Transcription Factor Database (TRANSFAC) program (*21*, *22*) was used to predict candidate TFs responsible for β*CBP* transactivation and cis-response elements (CREs) in the β*CBP* promoter/enhancer sequence. The analysis revealed that nine TFs had the potential to bind the promoter region of β*CBP* (fig. S4A). RNAi was performed to determine which of the *TFs* would enhance the transcription level of β*CBP* (fig. S4B). Results showed that the down-regulation of *ATF4*, *CREB-A*, *ATF2*, and *EGR1* genes led to a decrease in the expression of β*CBP* in the pronotum, suggesting that these genes may regulate the transcription of β*CBP* (Fig. 2B). Expression plasmids for these four genes were constructed using pAc5.1b, and a dual luciferase reporter assay was conducted to examine their impact on the transcriptional activity of β*CBP*. Only S2 cells overexpressing the ATF2 protein demonstrated a significant increase in the transcriptional activity of the β*CBP* promoter (Fig. 2C). Following that, a DNA probe targeting the region spanning −182 to −157 bp, which comprises the putative ATF2 CRE (TTGCGTAA), was used. S2 cells with overexpressed ATF-His protein were used to extract nuclear proteins. An electrophoretic mobility shift assay (EMSA) was used to confirm the binding of ATF2 to the ATF2 CRE region in the β*CBP* promoter. The probe showed binding affinity with the isolated nuclear proteins, and the shift band disappeared upon the addition of a cold probe (100 times more concentrated than the labeled probe) (Fig. 2D, lanes 2 and 3). However, the mutant probes with five nucleotides replaced did not have any effect on the shift band (Fig. 2D, lanes 4 and 5). No supershifted band was observed in the control or when incubated with mouse IgG (Fig. 2D, lanes 6 and 7). However, upon the addition of the His-tag antibody, a supershifted band emerged and the shifted band diminished (Fig. 2D, lane 8). Therefore, we concluded that ATF2 initiates the transcription of β*CBP* by binding the CRE-like region of the β*CBP* promoter.

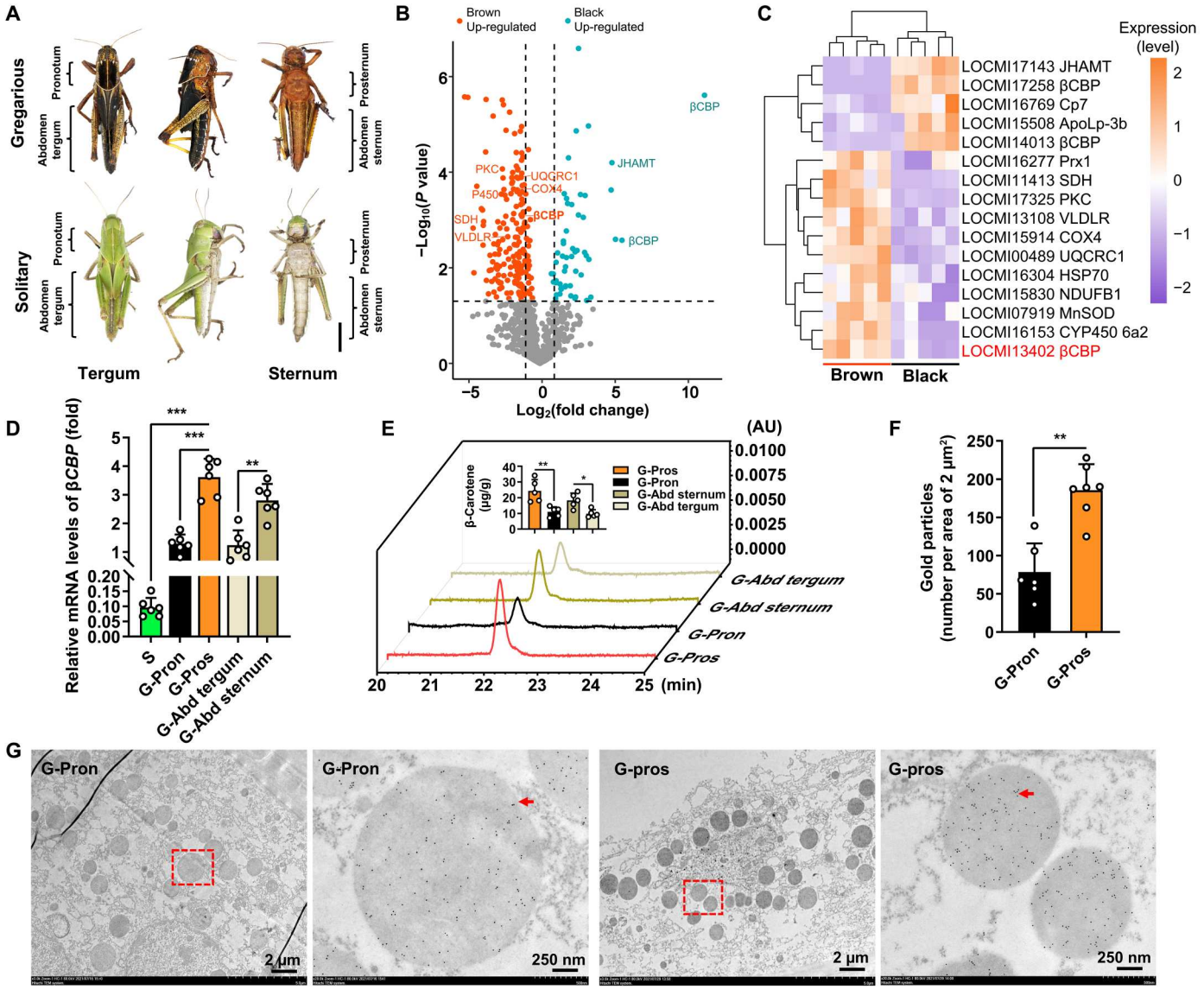

Fig. 1. βCBP and its binding to β-carotene directly contribute to the black and brown integuments of gregarious locusts. (**A**) Body color pattern of the fifth-instar gregarious and solitary locust nymphs. Scale bar, 1 cm. (**B**) Volcano plot of the quantified proteins from black and brown integuments. Red points represent up-regulated proteins in the brown integuments, while blue points represent up-regulated proteins in the black integuments [*P* value < 0.05, $\log_2$ fold change ($\log_2$FC) ≥ 1.0, *n* = 5]. The significantly DEPs associated with animal coloration are annotated in red and blue letters (*P* value < 0.01) and the possible functions of these significantly DEPs are shown in table S2. (**C**) Heatmap of probable animal coloration proteins from black and brown integuments. Orange and purple signals represent higher and lower levels (*P* value < 0.05 and $\log_2$FC ≥ 1.0, *n* = 5), respectively. The dendrograms indicate the hierarchical clustering of proteins and samples. (**D** and **E**) β*CBP* expression (D) and β-carotene content coupled with βCBP (E) in the S, G-Pron, G-Pros, G-Abdomen (Abd) tergum, and G-Abdomen (Abd) sternum of the fifth-instar locust nymphs. **P* < 0.05, ***P* < 0.01, and ****P* < 0.001, *n* = 5 or 6. AU, absorbance unit. (**F** and **G**) Subcellular distribution of βCBP in the G-Pron and G-Pros was investigated by immunoelectron microscopy. Images outlined with red squares are magnified, and the red arrow indicates the gold particles of βCBP located in the pigment granules. A number of gold particles in randomly selected pigment granules area in sections from various treatments were counted. ***P* < 0.01, *n* = 6 or 7. S, solitary locust nymph integument; G, Gregarious locust nymph integument; Pron, pronotum; Pros, prosternum. Data are presented as the means ± SDs. Asterisks indicate statistically significant differences based on two-tailed Student's *t* tests (**P* < 0.05, ***P* < 0.01, and ****P* < 0.001).

The ATF2 protein contains conserved domains in the N-terminal zinc finger (ZnF) and the basic leucine zipper (bZIP) (fig. S4, C to E). To examine the activation of the β*CBP* promoter by these domains, we constructed ATF2–wild type (WT) and three mutant plasmids. These plasmids were then transfected into S2 cells along with pGL4.10-β$CBP^{-184\ to\ +1}$, respectively. The results indicated that both ATF2-M1 and ATF2-M2 mutants reduced the activity of the β*CBP* promoter compared to the ATF2-WT control (Fig. 2E), confirming the importance of the ZnF-C2H2 and bZIP domains in transcriptional activation of the β*CBP* promoter.

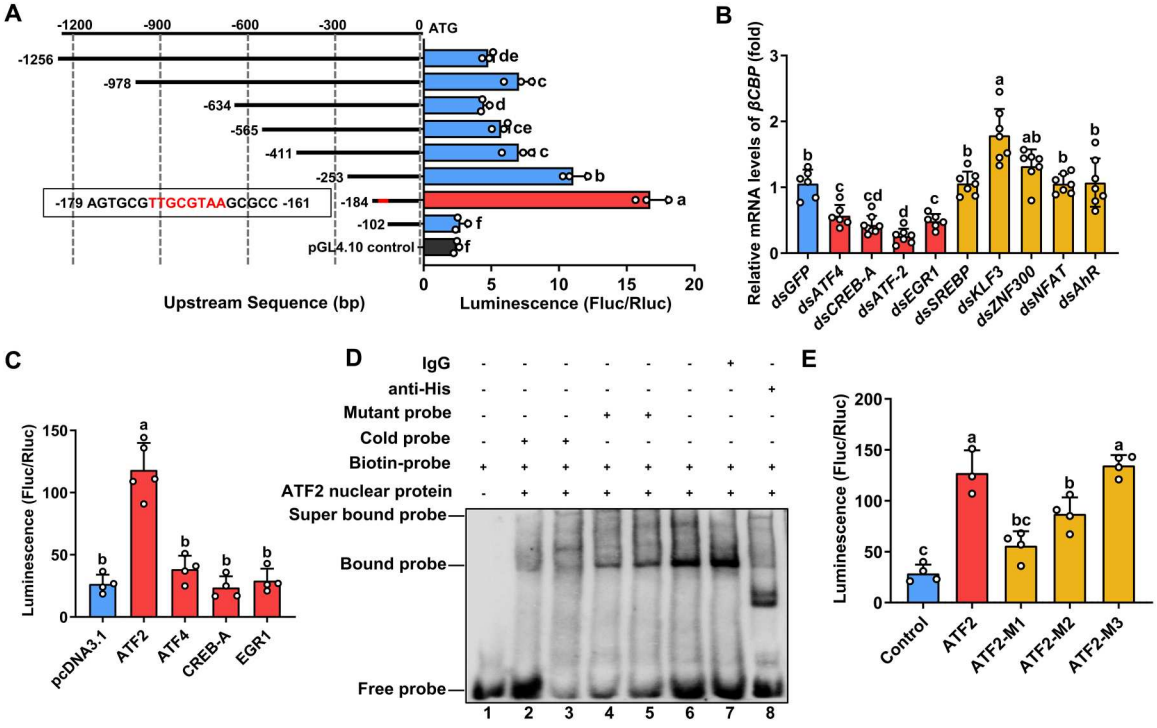

Fig. 2. The TF ATF2 increased the transcriptional activity of β*CBP* promoter. (**A**) Detection of transcriptional activity by a dual luciferase activity reporter assay system of β*CBP* promoters using progressive deletion constructs. The pGL4.10 plasmid was used as a control. S2 cells were cotransfected with pGL4.10 reporter plasmids carrying the indicated promoter regions and a reference reporter plasmid pGL4.73. $P < 0.05$, $n = 3$. (**B**) Detection of various TFs on the expression of β*CBP* via RNAi in vivo. *TF* knockdown (3 μg per nymph administered in the third-instar nymphs at day 2, three times over 48-hour intervals). *dsGFP* was used as a control. $P < 0.05$, $n = 6$ or 7. (**C**) Effects of four TFs on the activity of the β*CBP* promoter in dual luciferase reporter assays. pGL4.10-β$CBP^{-184\ to\ +1}$ and pGL4.73 were cotransfected into S2 cells with constructs of each TF in pAc5.1b. The empty vector pAc5.1b was used as a control. $P < 0.05$, $n = 4$ or 5. (**D**) Electrophoretic mobility shift assay (EMSA) of the binding of nuclear proteins extracted from S2 cells to the probe of the DNA region between −182 and −157 nt of the β*CBP* promoter. (**E**) Analysis of the functional domains of ATF2 using dual luciferase reporter assays. pGL4.10-β$CBP^{-184\ to\ +1}$ and pGL4.73 were cotransfected into S2 cells with pAc5.1b-ATF2 (ATF2), pAc5.1b-ATF2-M1 6– to 186–amino acid deletion (ATF2-M1), pAc5.1b-ATF2-M2 268– to 382–amino acid deletion (ATF2-M2), and pAc5.1b-ATF2-M3 457– to 577–amino acid deletion (ATF2-M3). pAc5.1b empty vector was used as a control. $P < 0.05$, $n = 3$ or 4. Fluc/Rluc represents the fold of firefly to *Renilla* luciferase activity. Data are presented as the means ± SDs. Different letters indicate multiple comparisons based on one-way ANOVA with Tukey's test ($P < 0.05$).

ATF2 controls βCBP expression, leading to body color transformation

To investigate the influence of ATF2 on the body coloration of gregarious locusts, we conducted an *ATF2* knockdown experiment to evaluate the impact on the expression of βCBP and the resulting body color phenotype. The black pronotum and the brown prosternum were both markedly lighter following *ATF2* knockdown (Fig. 3A and fig. S5A). Both ATF2 and βCBP expression levels decreased after the injection of *dsATF2* into gregarious locusts compared to the injection of *dsGFP* (Fig. 3B and fig. S5B). The reduction of β-carotene content in the pronotum was also observed following *ATF2* knockdown (Fig. 3C). Moreover, crowding of solitary locusts (CS) significantly increased β*CBP* expression (fig. S5C). In contrast, *dsATF2* injection into solitary locusts exposed to crowded conditions resulted in a significant decrease in β*CBP* expression compared to *dsGFP* injection (fig. S5C). Subsequent phenotypic analysis demonstrated that *ATF2* knockdown led to repression of the black-brown body color pattern formation under CS conditions (Fig. 3D and fig. S5D), which was further confirmed by Western blotting showing significantly reduced βCBP expression levels following *ATF2* knockdown in CS conditions (Fig. 3E). In addition, the β-carotene content of the pronotum significantly declined in locusts that underwent *ATF2* knockdown and CS treatment, compared to locusts that received *dsGFP* injection and CS treatment (Fig. 3F). Thus, ATF2 promotes β*CBP* transcription, resulting in the body color formation in gregarious locusts.

Pronotum and prosternum have different ATF2 phosphorylation levels

Although the transcript level of β*CBP* increased under crowding and decreased under isolation, *ATF2* expression showed no change across different population density (Fig. 4A). Moreover, there were no significant differences in *ATF2* transcript levels between solitary and gregarious integuments, as well as in its protein levels between the prosternum and the pronotum of gregarious locusts (Fig. 4, B and C). However, Western blotting analysis revealed the presence of two bands for ATF2 in both the pronotum and prosternum using Phos-tag SDS–polyacrylamide gel electrophoresis (SDS-PAGE) gel, with the upper band exhibiting higher expression in the prosternum compared to the pronotum (Fig. 4D). After lambda protein phosphatase (λPPase) treatment, the upper band of ATF2 in the prosternum disappeared, indicating its phosphorylated form (Fig. 4E). Phosphorylated ATF2 was more abundant in the prosternum's nuclear extracts compared to the

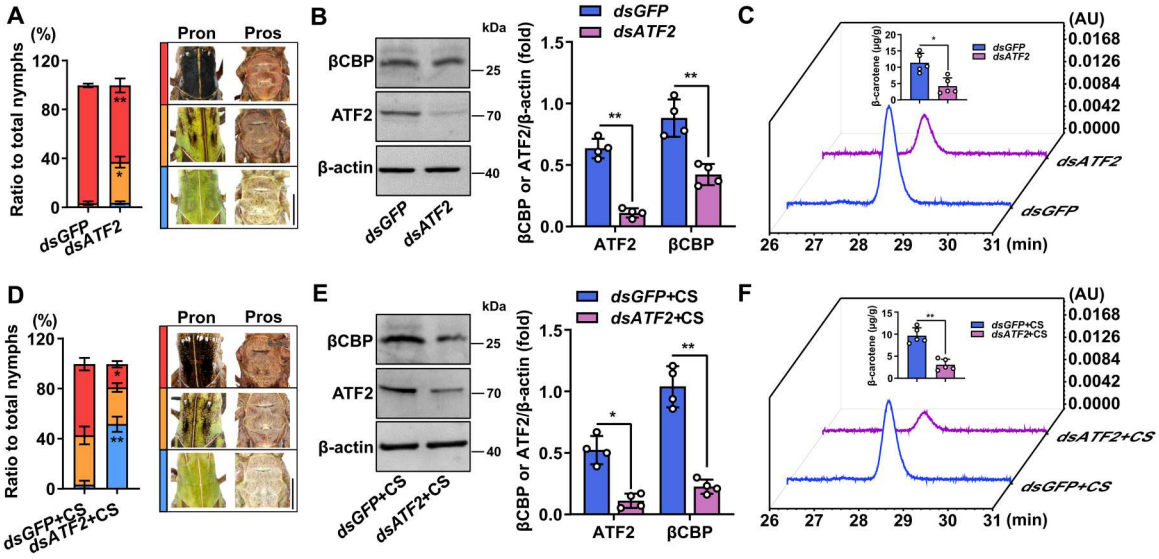

Fig. 3. ATF2 is required for the stimulation of βCBP expression and coloration. (**A**) Body color phenotypes of gregarious locust after RNAi exposure. *ATF2* knockdown (3 μg per nymph administered in the day two of the second-instar gregarious locust nymphs, four times over 48-hour intervals). Images were obtained from the fifth-instar nymphs. *dsGFP* was used as a control. Red box represents locusts with a notable black-brown pattern. Blue box represents locusts with a cryptic green color. Orange box represents the locusts with a body color that falls between the notable black-brown pattern and the cryptic green color. Scale bar, 0.5 cm. $^{*}P < 0.05$ and $^{**}P < 0.01$, $n = 3$. (**B**) Levels of ATF2 and βCBP in the Pron after *ATF2* knockdown in (A). $^{**}P < 0.01$, $n = 4$. (**C**) β-carotene content coupled with βCBP was evaluated in Pron after *ATF2* knockdown in (A) by HPLC. $^{*}P < 0.05$, $n = 5$. (**D**) Body color phenotypes of solitary locust after RNAi exposure and crowding. The RNAi operation in solitary locust nymphs was consistent with (A). CS indicates solitary locust nymphs after crowding. Images were obtained from the fifth-instar nymphs. Red, blue, and orange box indicates the same as (A). Scale bar, 0.5 cm. $^{*}P < 0.05$ and $^{**}P < 0.01$, $n = 3$. (**E**) Levels of ATF2 and βCBP in the Pron after *ATF2* knockdown and crowding in (D). $^{*}P < 0.05$ and $^{**}P < 0.01$, $n = 4$. (**F**) β-carotene content coupled with βCBP was evaluated in Pron after *ATF2* knockdown and crowding in (D) by HPLC. $^{**}P < 0.01$, $n = 5$. Data are presented as the means ± SDs. Asterisks indicate statistically significant differences based on two-tailed Student's *t* tests ($^{*}P < 0.05$ and $^{**}P < 0.01$).

pronotum, while nonphosphorylated ATF2 levels were lower in the prosternum's cytoplasm than the pronotum (Fig. 4F). These data indicated that phosphorylation is essential for ATF2 to translocate from the integument cytoplasm to the nucleus to bind to the β*CBP* promoter.

Immunostaining of gregarious locust integuments was performed to visualize the subcellular distribution of ATF2 in epidermal cells. Intriguingly, immunofluorescence staining showed differential localization of ATF2 in epidermal cells, with predominant cytoplasmic localization in the pronotum and nuclear localization in the prosternum (Fig. 4G). To confirm the variations in the extent and type of ATF2 phosphorylation between the prosternum and the pronotum, we conducted immunoprecipitation using anti-ATF2 antibodies, followed by protein collection and analysis. Protein extracts from the integuments showed the presence of phosphorylated serine/threonine (p-Ser/Thr) and phosphorylated threonine (p-Thr) in ATF2, with a higher abundance of p-Ser/Thr in the prosternum compared to the pronotum (Fig. 4, H and I). However, p-Thr did not differ between the two regions (Fig. 4I). Therefore, p-Ser ATF2 level was determined to be higher in the prosternum than in the pronotum.

PKC signaling promotes β*CBP* expression via ATF2 Ser^{327} phosphorylation

Given that ATF2 phosphorylation is regulated by several kinases, including protein kinase C (PKC) and mitogen-activated protein kinase (MAPK) (*23*–*26*), we aimed to investigate the activation of ATF2 by PKC and MAPKs in vitro. S2 cells were cotransfected with pGL4.10-β$CBP^{-184\ to\ +1}$ and pAc5.1b-ATF2 and then treated with a PKC inhibitor (H89) and inhibitors of the MAPK pathway including ERK (PD98059), p38 (SB203580), and JNK (SP600125). Compared with the negative control treated with dimethyl sulfoxide (DMSO), neither c-Jun N-terminal kinase (JNK) nor extracellular signal–regulated kinase (ERK) inhibitor treatments initiated β*CBP* transcriptional activation. In contrast, inhibition of the PKC and p38 pathways significantly decreased the reporter gene expression of β$CBP^{-184\ to\ +1}$, suggesting that the PKC and p38 pathways may positively regulate β*CBP* transcriptional activation (Fig. 5A). To determine the effect of these inhibitors on *ATF2* and β*CBP* expression in vivo, we separately injected these inhibitors into gregarious locusts. Unexpectedly, injection of a PKC inhibitor, but not a MAPK pathway inhibitor, significantly reduced β*CBP* transcription compared to the control injection with phosphate-buffered saline (PBS) (Fig. 5B). However, there was no difference observed in *ATF2* expression between these treatments (Fig. 5B). Thus, we concluded that the PKC pathway is involved in β*CBP* transcriptional activation.

To identify the phosphorylation sites of ATF2, we isolated purified ATF2 by immunoprecipitation with an anti-ATF2 antibody. The phosphorylation level of ATF2 decreased significantly after treatment with a PKC inhibitor, as determined by the anti–phospho-(Ser) PKC substrate (anti–pS-PKC substrate) polyclonal antibody, indicating that PKC kinase activates ATF2 phosphorylation at Ser. Meanwhile, βCBP expression was significantly decreased after PKC inhibitor treatment (Fig. 5C). The potential phosphorylation sites in locust ATF2 were predicted using NetPhos 3.1. On the basis of high-scoring serine phosphorylation of the PKC substrate, four serine residues (Ser^{327}, Ser^{406}, Ser^{518}, and Ser^{668}) were

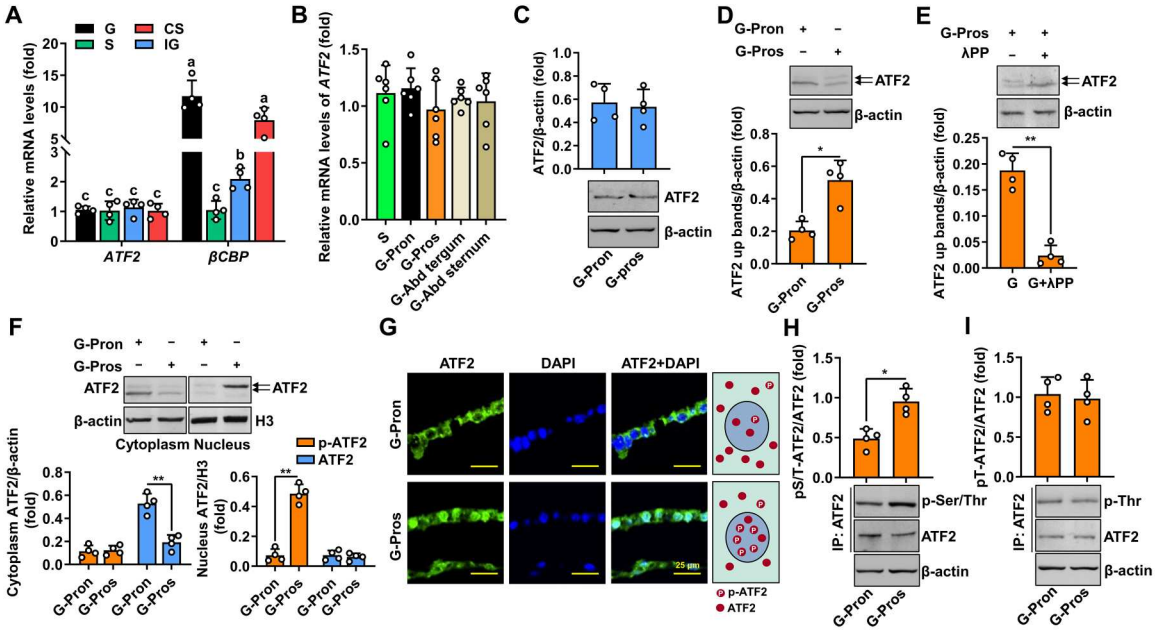

Fig. 4. ATF2 subcellular distribution and its phosphorylation levels at Serine differ between G-Pron and G-Pros. (**A**) *ATF2* and β*CBP* expression in the Pron of the fifth-instar locust nymphs. IG indicates gregarious nymphs after isolation. CS means solitary nymphs after crowding. $P < 0.05$, $n = 4$. (**B**) *ATF2* expression in the S, G-Pron, G-Pros, G-Abdomen tergum, and G-Abdomen sternum of the fifth-instar locust nymphs. $n = 6$. (**C**) ATF2 levels in G-Pron and G-Pros. 12% SDS-PAGE gel. $n = 4$. (**D**) Western blotting analysis of ATF2 in G-Pron and G-Pros by Phos-tag SDS-PAGE gel. $^*P < 0.05$, $n = 4$. (**E**) Verification of phospho-ATF2 by using protein extracts from G-Pros subjected to phosphatase λPPase treatment for 30 min. Phos-tag SDS-PAGE gel. $^{**}P < 0.01$, $n = 4$. (**F**) Western blotting analysis of ATF2 extracted from the cytoplasm and nuclei of G-Pron and G-Pros. Phos-tag SDS-PAGE gel. $^{**}P < 0.01$, $n = 4$. (**G**) Distribution analysis of ATF2 in G-Pron and G-Pros via immunohistochemistry. Rabbit polyclonal antibodies against ATF2 were used as the primary antibody. Green indicates ATF2 staining by the anti-ATF2 antibody. Blue indicates 4′,6-diamidino-2-phenylindole (DAPI) staining for nuclei. Schematic diagram showing ATF2 distribution in the cytoplasm and nuclei. Scale bars, 25 μm. (**H** and **I**) Ser phosphorylation of ATF2 differs in G-Pron and G-Pros. ATF2 protein was enriched from the epidermis using anti-ATF2 antibody-bound CNBr-activated Sepharose 4B. The phosphorylation of ATF2 was detected using anti–phospho-serine/threonine polyclonal antibodies (p-Ser/Thr) and anti–phospho-threonine polyclonal antibodies (p-Thr). $^*P < 0.05$, $n = 4$. IP, immunoprecipitation. Data are presented as the means ± SDs. Different letters indicate multiple comparisons of significant differences based on one-way ANOVA followed by Tukey's test ($P < 0.05$). Asterisks indicate statistically significant differences based on two-tailed Student's *t* tests ($^*P < 0.05$ and $^{**}P < 0.01$).

suggested as potential phosphorylation sites (fig. S6A). Liquid chromatography tandem mass spectrometry (LC-MS/MS) analysis using proteins isolated from the prosternum showed that ATF2 was phosphorylated at Ser^{45}, Ser^{327}, and $Thr^{55/57}$ (fig. S6, B to D). To validate the serine phosphorylation sites that activate β*CBP* transcription, pGL4.10-β$CBP^{-184\ to\ +1}$ was transfected into S2 cells overexpressing ATF2 WT or ATF2 mutants (ATF2 S45A, ATF2 S327A, ATF2 S406A, ATF2 S518A, and ATF2 S668A). There was no significant difference in luciferase activity between ATF2 WT and ATF2 S45A, ATF2 S406A, ATF2 S518A, and ATF2 S668A mutants. However, compared with ATF2 WT, the ATF2 S327A mutant significantly decreased reporter gene expression driven by the promoter of β*CBP* (Fig. 5D). Thus, we concluded that the PKC pathway activates the Ser^{327} phosphorylation of ATF2 and subsequently promotes the transcriptional activation of the β*CBP* promoter.

PKCα phosphorylates ATF2 to promote its nuclear translocation

Considering the existence of multiple isoforms of PKC (fig. S7), we conducted an RNAi screening of genes encoding *PKC*α (GenBank: MN793141), *PKC*δ (GenBank: MN793140), *PKC*ε (GenBank: MN793143), and *PKC*ι (GenBank: MN793142) in gregarious locusts to determine which isoform could catalyze ATF2 phosphorylation. Only *PKC*α silencing in these *PKC* isoforms decreased β*CBP* expression (Fig. 6A). We generated an anti–phospho-ATF2 (Ser^{327}) (referred to as anti–pS-ATF2) antibody and confirmed its specificity through Western blotting analysis using proteins extracted from the prosternum of fifth-instar gregarious locust nymphs treated with phosphatase λPPase (fig. S8). Western blotting analysis using anti–pS-ATF2 showed that the depletion of *PKC*α significantly inhibited ATF2 phosphorylation (Fig. 6B). In contrast, knockdown of *PKC*ε, *PKC*δ, or *PKC*ι showed no significant differences in ATF2 phosphorylation and β*CBP* expression compared to the *dsGFP* negative control (Fig. 6B and fig. S9). Moreover, there was no change in the abundance of ATF2 after knockdown of each *PKC* isoform (Fig. 6B). As for the phenotypes, the black pronotum and brown prosternum faded after *PKC*α knockdown (Fig. 6C). Immunohistochemistry results demonstrated that ATF2 was primarily localized in the cytoplasm of the prosternum and that the pS-ATF2 signal decreased after treatment with *dsPKC*α (Fig. 6D), confirming the essential role of PKCα in ATF2 phosphorylation and its translocation from the cytoplasm to the nucleus linked with variations in body color.

The β-carotene content in the pronotum was detected to decrease after *PKC*α knockdown (Fig. 6E). In vivo chromatin immunoprecipitation (ChIP) analysis was performed using an anti–pS-ATF2 antibody and nuclear extracts from the prosternum, which had higher ATF2 phosphorylation levels. The β*CBP* promoter

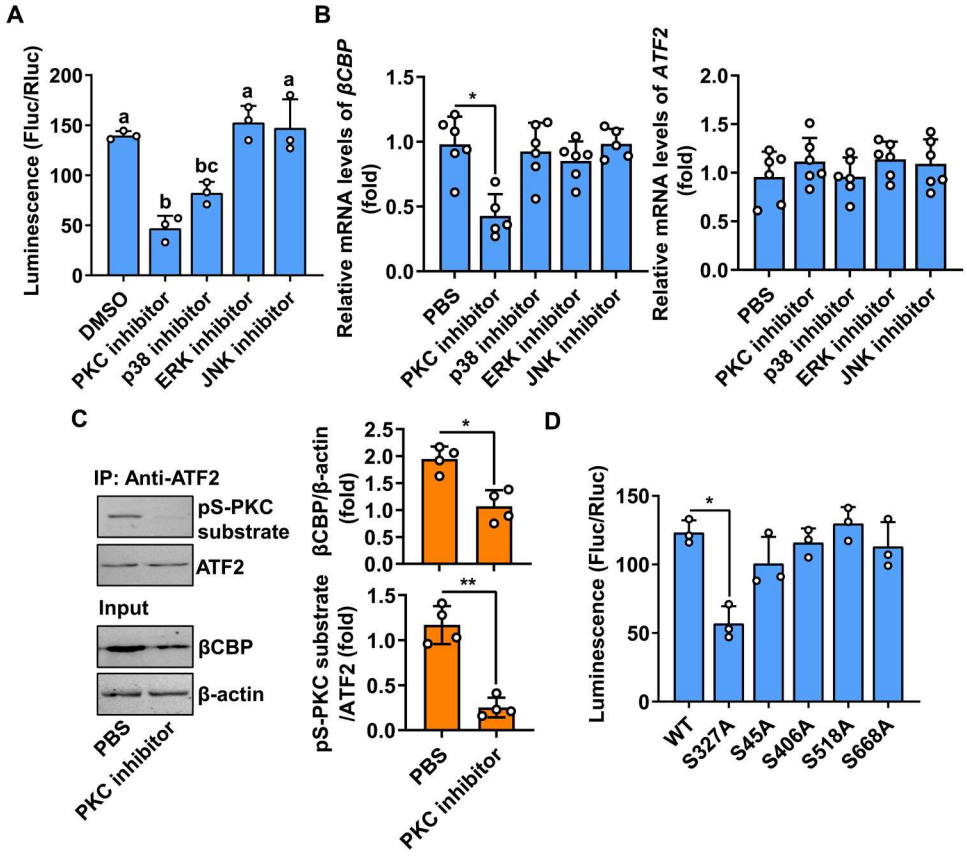

Fig. 5. The PKC signaling pathway phosphorylates ATF2 at Ser^{327} to promote β*CBP* expression. (**A**) Effects of various kinase inhibitors on the β*CBP* promoter via dual luciferase reporter assays. pGL4.10-β*CBP* $^{-184\ to\ +1}$ and pGL4.73 were cotransfected into S2 cells overexpressing ATF2 and incubated with the PKC inhibitor (20 μM), ERK inhibitor (30 μM), p38 inhibitor (30 μM), or JNK inhibitor (30 μM). DMSO was used as a control. $P < 0.05$, $n = 3$. (**B**) Relative levels of β*CBP* and *ATF2* in the Pron of the fifth-instar gregarious locust nymphs injected with various inhibitors. Inhibitor (50 μM per nymph) was injected into the mid-third instar gregarious locust nymphs twice over 48-hour intervals. *$P < 0.05$, $n = 5$ or 6. (**C**) Verification of ATF2 phosphorylation at serine stimulated by PKC. PKC inhibitor (50 μM per nymph) was injected into the mid-third instar gregarious locust nymphs twice over 48-hour intervals. PBS was used as a control. ATF2 protein was enriched from the Pron of the fifth-instar gregarious locust nymphs using anti-ATF2 antibody-bound CNBr-activated Sepharose 4B. The phosphorylation of ATF2 was detected using anti–phospho-(Ser) PKC substrate (pS-PKC substrate) polyclonal antibodies. *$P < 0.05$ and **$P < 0.01$, $n = 4$. (**D**) Expression is driven by the promoter of β*CBP* in the presence of various constructs. pGL4.10-β*CBP* $^{-184\ to\ +1}$ and pGL4.73 were cotransfected into S2 cells with ATF2 (WT), ATF2 S45A, ATF2 S327A, ATF2 S406A, ATF2 S518A, and ATF2 S668A, respectively. *$P < 0.05$, $n = 3$. Fluc/Rluc represents the fold of firefly to *Renilla* luciferase activity. Data are presented as the means ± SDs. Asterisks indicate statistically significant differences based on two-tailed Student's *t* tests (*$P < 0.05$ and **$P < 0.01$). Different letters indicate multiple comparisons of significant differences based on one-way ANOVA followed by Tukey's test ($P < 0.05$).

region enriched by anti–pS-ATF2 was decreased after *PKC*α suppression (Fig. 6F). Given the essential role of PKCα and pS-ATF2 in facilitating β*CBP* expression, we explored the association of PKCα and ATF2 between the pronotum and the prosternum. A coimmunoprecipitation assay showed that ATF2 coimmunoprecipitated more PKCα in the prosternum than in the pronotum using the anti-ATF2 antibody (fig. S10A), indicating that high levels of ATF2 phosphorylation in the prosternum depend on high PKCα and ATF2 interactions. The integuments of gregarious locusts turned red (fig. S10B) when the expression of β*CBP*, the content of pigment β-carotene, and the β*CBP* promoter region enriched by anti–pS-ATF2 from the pronotum were increased after PKCα agonist exposure (fig. S10, C to E). Therefore, we concluded that ATF2 phosphorylation promotes β*CBP* transcription and β-carotene pigmentation.

To test whether the interaction of ATF2 and PKCα can respond to changes in population density, we extracted proteins from the prosternum of locusts during a time-course phase transition (isolation of gregarious locusts was denoted as IG, and crowding of solitary locusts was denoted as CS) for two stadia. Immunoprecipitation using an anti-ATF2 antibody followed by Western blotting analysis with antibodies against PKCα revealed that more PKCα interacted with ATF2 in the prosternum of gregarious locusts, and the association between PKCα and ATF2 decreased in the prosternum of IG without changing the protein expression of PKCα and ATF2 in the input (fig. S11A). The interaction between PKCα and ATF2 was increased in the prosternum of CS, in contrast to the low level of PKCα interaction with ATF2 in the prosternum of solitary locusts (fig. S11B). Both the pS-ATF2 and βCBP contents from the prosternum of gregarious locusts were significantly higher than those of the prosternum of solitary locusts. Moreover, both the pS-ATF2 and βCBP contents were increased after CS and were decreased after IG. However, ATF2 exhibited no change in these samples from the time-course treatments (fig.

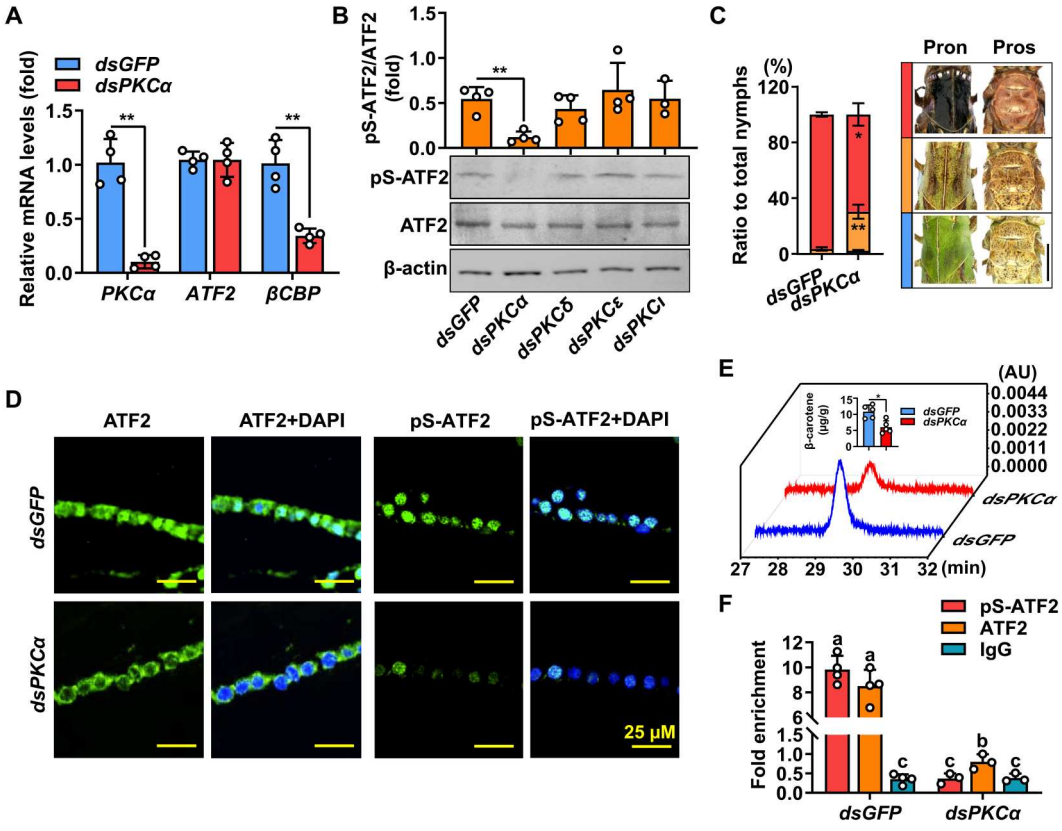

Fig. 6. PKCα facilitates ATF2 phosphorylation, translocation into the nucleus, β*CBP* expression and coloration. (**A**) β*CBP* and *ATF2* mRNA levels after *PKC*α knockdown in Pron. *PKC*α knockdown (3 μg per nymph administered in the day 2 of the second-instar gregarious locust nymphs, four times over 48-hours intervals). *dsGFP* was used as a control. $^{**}P < 0.01$, $n = 4$. (**B**) ATF2 phosphorylation levels in Pron after *PKC* isoform knockdown. $^{**}P < 0.01$, $n = 3$ or 4. (**C**) Body color phenotypes of gregarious locust nymphs after RNAi exposure. Images were obtained on the fifth-instar nymphs after RNAi exposure. Red box represents locusts with a notable black-brown pattern. Blue box represents locusts with a cryptic green color. Orange box represents locusts with a body color that falls between the notable black-brown pattern and the cryptic green color. Scale bar, 0.5 cm. $^{*}P < 0.05$ and $^{**}P < 0.01$, $n = 3$. (**D**) Immunohistochemistry of ATF2 and pS-ATF2 in Pros after *PKC*α knockdown. Green denotes ATF2 or pS-ATF2 staining by anti-ATF2 antibodies or anti–phospho-ATF2 (Ser^{327}) antibodies. Blue denotes DAPI staining for nuclei. Scale bars, 25 μm. (**E**) β-carotene content coupled with βCBP was evaluated in Pron after *PKC*α knockdown by HPLC. $^{*}P < 0.05$, $n = 5$. (**F**) ChIP assays show that *PKC*α knockdown repressed the relative precipitation of the β*CBP* promoter region in Pros. pS-ATF2, phospho-ATF2 (Ser^{327}) antibodies; ATF2, ATF2 antibodies; IgG, nonspecific rabbit IgG control. $P < 0.05$, $n = 3$ or 4. Pron: The fifth-instar gregarious locust nymphs pronotum. Pros: The fifth-instar gregarious locust nymphs prosternum. Data are presented as the means ± SDs. Asterisks indicate statistically significant differences based on two-tailed Student's *t* tests ($^{*}P < 0.05$ and $^{**}P < 0.01$). Different letters indicate multiple comparisons of significant differences based on one-way ANOVA followed by Tukey's test ($P < 0.05$).

S11C). Thus, we concluded that crowding treatments can stimulate ATF2 phosphorylation at Ser^{327} by enhancing the PKCα and ATF2 interaction and promote βCBP expression via pS-ATF2 binding to the β*CBP* promoter.

pS-ATF2–mediated β*CBP* transcription determines the body color pattern of gregarious locusts

As ATF2 phosphorylation induced by PKCα was concomitant with β*CBP* transcription, we attempted to determine the relationship between pS-ATF2 and βCBP in the pronotum and prosternum of gregarious locusts. Immunohistochemistry analysis using pS-ATF2 and βCBP antibodies showed that pS-ATF2 was localized in the nucleus, and both pS-ATF2 and βCBP contents were higher in the prosternum than in the pronotum. In contrast, the pronotum of solitary locusts, which served as a negative control, exhibited considerably low levels of both pS-ATF2 and βCBP (Fig. 7A). Subsequent Western blotting analysis confirmed the accumulation of pS-ATF2 in the nucleus of the prosternum cells (Fig. 7B). Furthermore, the abundance of phosphorylated ATF2 and βCBP was significantly higher in the prosternum compared to the pronotum but with total ATF2 being constant in both integument parts (Fig. 7C). Therefore, we concluded that differential phosphorylation but not the differential expression of ATF2 plays a crucial role in βCBP expression. ChIP assays in vivo confirmed that, compared with the pronotum, the prosternum exhibited a higher enrichment of pS-ATF2 bound to the promoter sequence of β*CBP*, which aligns with the higher levels of pS-ATF2 in the prosternum (Fig. 7D). Together, ATF2 phosphorylation is pivotal in triggering β*CBP* transcription for the body coloration in gregarious locusts.

DISCUSSION

Our present study revealed that variations of βCBP expression and β-carotene content across different parts of body result in the

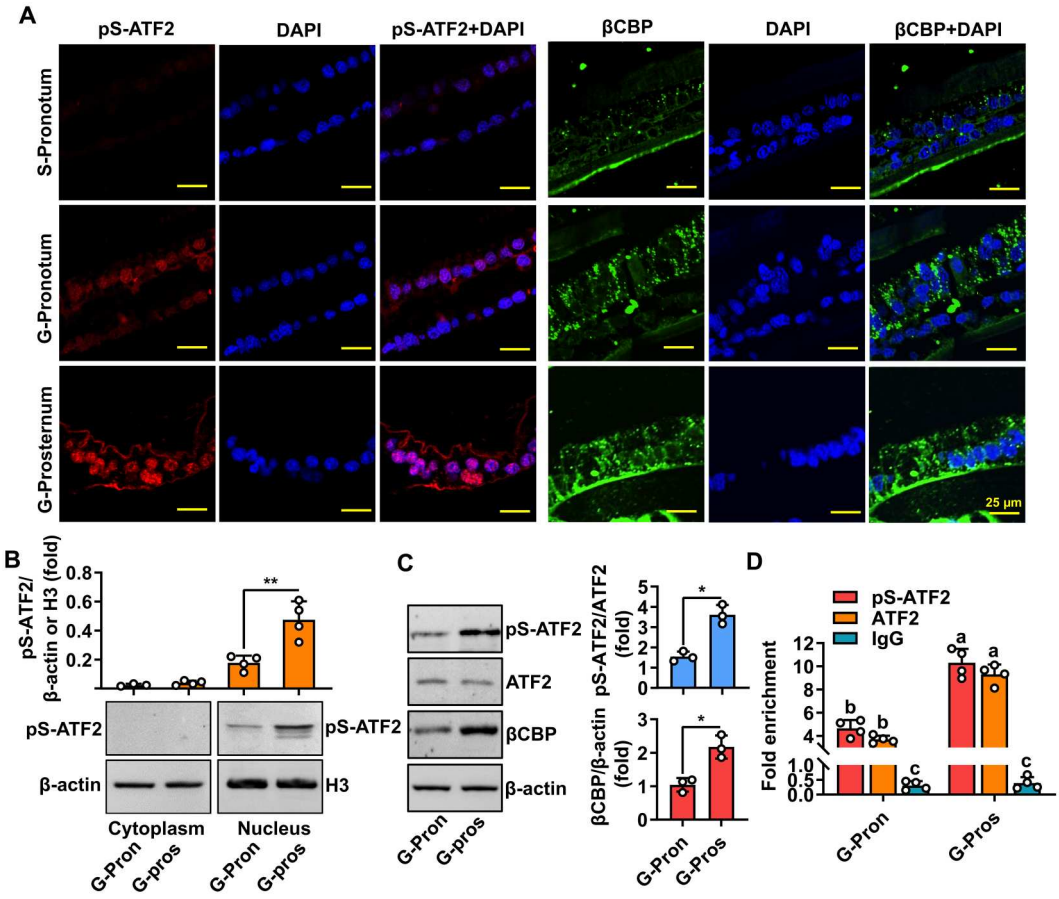

Fig. 7. pS-ATF2 extent is required for its role in stimulating β*CBP* transcription. (**A**) Immunohistochemistry shows the distribution and abundance of βCBP and phosphorylated ATF2 in S-Pron, G-Pron, and G-Pros from the fifth-instar locust nymphs. Red denotes phosphorylated ATF2 detected using anti–pS-ATF2 antibodies, green denotes βCBP detected using anti-βCBP antibodies, and blue denotes nuclei stained using DAPI. Scale bars, 25 μm. (**B**) Western blotting analysis of pS-ATF2 extracted from the cytoplasm and nuclei of G-Pron and G-Pros from the fifth-instar locust nymphs. $^{**}P < 0.01$, $n = 4$. (**C**) Western blotting analysis of pS-ATF2, ATF2, and βCBP levels in G-Pron and G-Pros from the fifth-instar locust nymphs. $^{*}P < 0.05$, $n = 3$. (**D**) ChIP assays show the relative precipitation of the β*CBP* promoter region in G-Pron and G-Pros from the fifth-instar locust nymphs. $P < 0.05$, $n = 4$. S-Pron, solitary locust nymph pronotum; G-Pron, Black integument of gregarious locust nymph pronotum; G-Pros, Gregarious locust nymph prosternum. Data are presented as the means ± SDs. Asterisks indicate statistically significant differences based on two-tailed Student's *t* tests ($^{*}P < 0.05$ and $^{**}P < 0.01$). Different letters indicate multiple comparisons of significant differences based on one-way ANOVA followed by Tukey's test ($P < 0.05$).

conspicuous coloration of a black back and brown venter in gregarious locusts. This distinct body coloration serves as a warning signal to predators, which prefer to consume green solitary locusts rather than black-brown gregarious ones (*10*). Many animals display darkening of dorsal pigmentation and distinct upper and lower body coloration (*27*, *28*) as an adaptive mechanism to evade predation in their natural habitats (*29*). Warning coloration provides a more conspicuous color contrast and enhances innate biases against colors such as red, yellow, and black, indicating potential toxicity to predators (*30*). The association between prey color and toxicity is potentiated, leading to improved retention of learned associations (*31*). Notably, the contrasting body color of gregarious locusts is closely associated with olfactory aposematic signal and the toxin HCN (*10*), making them less attractive to predators and increasing their likelihood of survival. When migratory locusts perceive a threat, they exhibit startle behavior, involving rapid escape jumping (*32*, *33*), and convert the PAN to HCN (*10*). Similarly, the monarch butterfly *D. plexippus* uses its unique black and orange pattern to warn predators of the highly toxic cardiac glycosides stored within its body (*12*). The poison frog *Dendrobates tinctorius* uses a combination of colors and pattern elements to create a highly conspicuous and recognizable signal that is easily perceived by predators at close range while minimizing detectability by distant observers (*34*). In conclusion, the incorporation of black with other colors is a way for animals to advertise their toxicity, unpleasantness, or danger to predators (*12*, *35*, *36*). In addition, PAN and HCN may serve as honest signals to deter cannibalism in gregarious locusts (*37*). This notable coloration linked with toxin can serve as a deterrent to natural predators and reduce the risk of preys being attacked (*12*, *34*).

The black-brown body color pattern of gregarious locusts may serve as an identifier in conspecific interaction and communication. Specifically, the epidermal cells of desert locusts (*Schistocerca gregaria*) produce a yellow protein that binds to β-carotene, generating bright yellow coloration in sexually mature males and functioning as an intrasexual warning signal (*38*). Further, organisms can use

spatial separation of signals for private communication purposes, whereby different parts of the body convey different information (*39*). Similarly, the distinctive black-brown coloration on the gregarious nymphs can be perceived by conspecifics viewing laterally. The absence of a bellwether effect has led to the suggestion that special coloration plays a crucial role in the band marching and migration of locusts. In the desert locusts, visual feature recognition and discrimination are crucial during band marching (*40*). The black-brown body color pattern may also be critical for collective movement, although further inquiry is warranted.

Understanding the distribution of pigments and their binding proteins in integuments is crucial in comprehending the creation of conspicuous coloration. Our research has revealed that differences in the accumulation of the βCBP–β-carotene complex are responsible for the unique coloration observed in migratory locusts. The locusts′ body color can respond to signals of population density, which stimulate the transcriptional activity of the ATF2 TF. ATF2 can accurately control the expression levels of β*CBP* by transcriptional activation in the body coloration of gregarious locusts. Although the RNAi in vivo of the other three TFs (*ATF4*, *CREB-A*, and *EGR1*) led to the down-regulation of β*CBP* mRNA, cellular experiments in vitro did not demonstrate an increase in the transcriptional activity of the β*CBP* promoter. This is possibly because these three TFs do not directly initiate β*CBP* transcription by binding to the β*CBP* promoter in vivo but instead indirectly regulate its transcription through the regulation of *ATF2*′s upstream target genes. ATF2, a member of the bZIP TF family, is activated by various stimuli, including growth factors, ultraviolet radiation, and cytokines, regulating normal cellular growth, development, apoptosis, and the cellular response to stress (*41*). The pigmentation differences affected by environmental cues can be mediated by some TFs and patterning genes (*15*–*18*, *42*). Although some TFs have been confirmed to control the composition of insect body color, most studies have only analyzed species body color diversity controlled by TFs at the genomic evolutionary level (*18*, *43*). For instance, *spätzle3*/*Toll-8* controls the melaninization process and striped pattern formation in the silkworm dominant mutant Zebra (*44*), and *Pannier* contributes to melanic pattern polymorphism on the elytra of the harlequin ladybird, *Harmonia axyridis* (*18*). However, few studies have reported that body color plasticity results from the precise regulation of TFs within the same generation in conspecifics. Our study here demonstrates that the differential distributions of the βCBP–β-carotene complex are regulated by ATF2, which determines the black pronotum and brown prosternum coloration pattern. The unique body color pattern of gregarious locusts, controlled by ATF2 and βCBP, can rapidly respond to changes in population density. This finding extends our understanding of contrast body coloration achieved by altering the levels of a single TF and effector.

ATF2 phosphorylation is fundamental for the transcriptional activation of β*CBP* during the body color formation process in gregarious locusts. Our studies revealed that the spatial heterogeneity of phosphorylated ATF2 and βCBP expression confers the black tergum and brown sternum in gregarious locusts. We identified Ser^{327} as the only site on ATF2 that positively affects β*CBP* transcriptional activation. The other sites, including Ser^{45}, Ser^{406}, Ser^{518}, and Ser^{668}, do not affect transcriptional activation. Our experiments showed that p38 stimulates β*CBP* transcription in S2 cells without affecting the level of β*CBP* in gregarious locusts. This difference could be due to the different experimental conditions in vitro and in vivo. Other forms of ATF2 phosphorylation could potentially be involved in β*CBP* transcriptional activation. Notably, the phosphorylation sites $Thr^{53/55}$ and the surrounding region of locust ATF2 are conserved across various species, including humans (fig. S4E), implying their evolutionary significance for gene transcription in various cellular processes. Our findings suggest that ATF2 $Thr^{53/55}$ may be phosphorylated by p38 to activate β*CBP* transcription in S2 cells. Although certain phosphorylation sites in ATF2 are conserved, the respective sites of phosphorylation and the responsible kinases vary across different species (*23*–*26*, *45*). For instance, $Thr^{69/71}$ phosphorylation in ATF2 is induced by insulin/epidermal growth factors for its transcriptional activation via p38 (*46*) or JNK (*26*, *47*) in HeLa cells and fibroblasts. Nevertheless, we cannot exclude the possibility of other types of ATF2 phosphorylation being involved in β*CBP* transcriptional activation in gregarious locusts. Further investigations are warranted to confirm this hypothesis.

ATF2 subcellular localization is regulated by PKC signaling and plays a crucial role in numerous cellular functions. ATF2 Ser^{327} phosphorylation and subsequent nuclear translocation were enhanced by PKCα under population density stimulation in our study. In addition, the PKC inhibitor bisindolylmaleimide has been shown to reduce skin pigmentation in pigmented guinea pigs, indicating that PKC activity is involved in skin pigmentation (*48*). In gregarious locusts, a PKCα agonist activates ATF2 Ser^{327} phosphorylation, which promotes β-carotene pigmentation in the integument. Changes in body color are closely linked to population density signals in locusts (*7*), with crowding treatment resulting in a rapid increase in ATF2 phosphorylation, while isolation treatment decreased ATF2 phosphorylation. This rapid posttranslational regulation of ATF2 contributes to the quick response of locusts to changes in population densities. Moreover, the precise regulation of the coloration pattern of gregarious locusts is achieved through the finely tuned regulation of βCBP location and extent, which is maintained by ATF2 phosphorylation. Consequently, our research has revealed the underlying mechanism involved in the development and maintenance of the distinct coloration patterns observed in swarm and group defense.

Our study delves into the molecular mechanism responsible for the formation of aposematic coloration in locusts. We found that the interaction between PKCα and ATF2 serves as a response to extrinsic signals of population densities, enabling swift ATF2 phosphorylation modification and enhancing locust defense and adaptation to predation risks and environmental changes (Fig. 8). Our findings demonstrate an epigenetic mechanism where phosphorylated ATF2 regulates βCBP expression in a density-, ontogenetic-, and skin region-specific manner, shedding light on how extrinsic signals of population densities contribute to multifunctional signaling and phenotypic plasticity during evolution.

MATERIALS AND METHODS

Insects and treatments

Migratory locusts (*Locusta migratoria*) from a colony maintained at the Institute of Zoology at the Chinese Academy of Sciences were reared in our laboratory under an L14:D10 photoperiod at 30° ± 2°C with a diet of fresh wheat seedlings and bran as previously reported (*10*). Gregarious nymphs were reared in cages (40 cm by 40

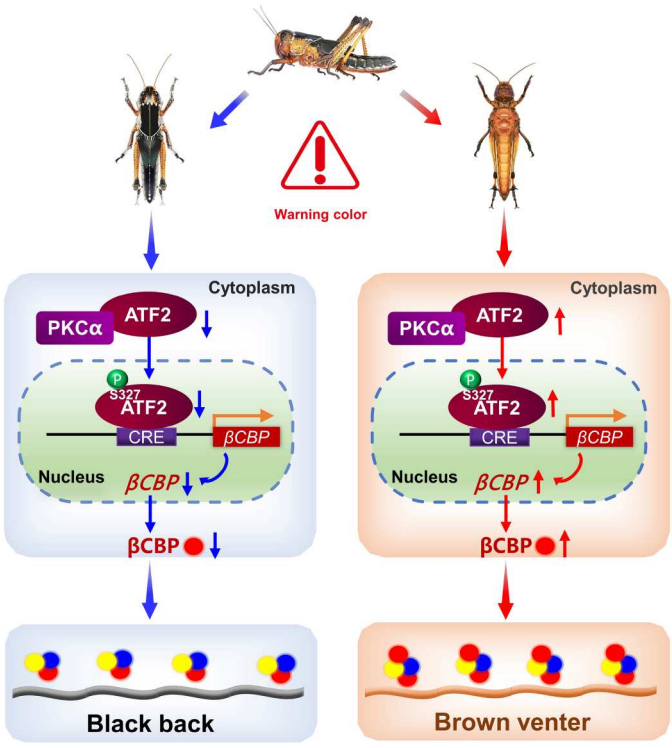

Fig. 8. A model of ATF2 phosphorylation regulating βCBP-mediated warning coloration in gregarious locusts. Gregarious locusts exhibit a sharp contrast body color pattern between the black tergum and brown sternum at high population densities. High population density promotes ATF2 phosphorylation at Ser^{327} via PKCα. Phosphorylated ATF2 migrates from the cytoplasm to the nucleus for β*CBP* promoter binding and subsequently triggers β*CBP* expression, which enhances the red color pigment β-carotene and βCBP complex. The black tergum emerges from the superposition of the red βCBP–β-carotene complex onto the solitary green background based on the physically trichromatic theory. In contrast, higher levels of phosphorylated ATF2 activate β*CBP* transcription, which causes brown coloration in the sternum with redder βCBP–β-carotene complexes. Dots with different colors indicate different pigment binding protein-pigment complexes (orange, βCBP; blue, blue-related pigment binding protein; yellow, yellow-related pigment binding protein) in locust epidermal cells. The blue arrows indicate low levels, and the red arrows indicate high levels.

cm by 40 cm) with 500 insects per cage. Solitary nymphs were individually reared in cages (10 cm by 10 cm by 25 cm) supplied with charcoal-filtered compressed air.

For the isolation treatment (IG), the third-instar gregarious nymphs were separately reared under the solitary conditions described above. For the crowding treatment (CS), 15 of the third-instar solitary nymphs were reared together in a small cage (10 cm by 10 cm by 10 cm). For inhibitor treatments, third-instar gregarious nymphs were injected with 50 μM per nymph PKC inhibitor (Gö6976, Selleck), ERK inhibitor (PD98059, Cell Signaling Technology), p38 inhibitor (SB202190, Cell Signaling Technology), or JNK inhibitor (SP600125, Cell Signaling Technology) twice over 48-hour intervals. All animal experiments were conducted under the license of the Animal Experimental Committee of the Institute of Zoology (AECIOZ), Chinese Academy of Science (IOZ20170071).

Proteomic and LC-MS/MS analysis

For LC-MS/MS analysis, the total protein from the black and brown integuments of thorax and abdomen of fifth-instar gregarious nymphs was extracted and digested with trypsin. Each protein sample was subjected to LC-MS/MS analysis using the label-free quantitative proteomic approach by PTM Biolabs (Hangzhou, China).

All raw data for each sample from LC-MS/MS were searched using the MaxQuant 1.5.3.17 software with a false discovery rate of 1% for identification and quantitation analysis against the locust database (http://159.226.67.243/download.htm). The volcano plot and heatmap were generated by RStudio software.

βCBP structure modeling and β-carotene docking

The protein structure was predicted using iterative threading assembly refinement (I-TASSER) (https://zhanglab.ccmb.med.umich.edu/I-TASSER/), and the binding pockets of protein models were predicted by DeepSite (https://playmolecule.com/deepsite/) and Proteins*Plus* (https://proteins.plus). Molecular docking was conducted via Autodoc Vina (https://vina.scripps.edu), and a binding energy lower than −2.5 kcal was selected as a model. The Protein-Ligand Interaction Profiler tool (https://plip-tool.biotec.tu-dresden.de/plip-web/plip/index) was used to predict the interaction forces of the protein-ligand model, and the final figures were prepared with the PyMOL program.

Quantitative reverse transcription PCR

Total RNA was extracted from the integuments using TRIzol reagent (Invitrogen), and cDNA was reverse transcribed using the PrimeScript RT Reagent Kit with gDNA Eraser (TaKaRa). Quantitative reverse transcription (qRT-PCR) was performed using SYBR Green Real-time PCR Master Mix (Tiangen) with a LightCycler 480 instrument (Roche). Relative expression levels were calculated using the $2^{-\Delta\Delta Ct}$ method and normalized to β-*actin*. The primers used for RNAi and qRT-PCR are listed in table S3. All experiments were performed for six biological replicates.

The antibodies used in this study

Monoclonal anti–β-actin antibody (AC026, ABclonal Technology, Wuhan, China), polyclonal anti-H3 antibodies (ab1791, Abcam, Cambridge, UK), polyclonal anti-βCBP antibodies (*14*), and polyclonal rabbit antibodies against *L. migratoria* ATF2 (GenBank: OQ360058) and PKCα (GenBank: QNS30453) were prepared in our laboratory using recombinant protein from *Escherichia coli* to immunize rabbits. Briefly, fragments encoding portions of ATF2 (amino acids 190 to 360 and 490 to 626) or PKCα (amino acids 165 to 315) were amplified and fused with pET-28a (Promega) to produce the recombinant protein in *E. coli* rosette cells by 0.1 mM isopropyl β-D-thiogalactoside induction. The target protein was purified using a Ni^{2+}-NTA affinity column (GE Healthcare) and served as an antigen to generate rabbit polyclonal antibodies with ABclonal Technology (Wuhan, China). The polyclonal antibodies against pS-ATF2 were generated by GenScript (Nanjing, China). Antibodies against p-Ser/Thr, pS-PKC substrate, and p-Thr were purchased from Abcam and Cell Signaling Technology.

Immunoelectron microscopy

Integuments were fixed with 2.5% glutaraldehyde in 0.1 M PBS (pH 7.4) at 4°C overnight. Samples were dehydrated in a graded alcohol

series, followed by embedding in LR White resin. Ultrathin sections were cut and placed onto 50-mesh copper grids and then blocked with PBS containing 1% bovine serum albumin (BSA), 0.2% Tween 20, and 0.2% gelatin. Sections were incubated with anti-βCBP antibodies (1:1000) as primary antibodies and 10-nm gold-conjugated goat anti-rabbit immunoglobulin G (IgG) (1:1000) as secondary antibodies. After staining with 2% neutral uranyl acetate, βCBP labeled with 10-nm gold was visualized through a JEM-1400 transmission electron microscope (JEOL, Tokyo, Japan). Gold particles were counted from three randomly selected pigment granules in sections of three biological replicates.

β-Carotene quantification

The β-carotene content of the pronotum and prosternum from gregarious nymphs was quantified via reverse-phase high-performance LC (HPLC) and diode array detector according to the methods of a previous research article (*14*). Briefly, integuments of locust nymphs were homogenized and lysed in lysate buffer and incubated with βCBP antibodies and Protein A Sepharose at 4°C overnight. The samples were sonicated in a buffer containing a mixture of *n*-hexane, ethanol, and acetone (2:1:1, v/v/v) and then centrifuged. The supernatant and the ether extract of the bottom residual solution were collected and dried using a lyophilizer. The dried residue was dissolved in a mix of equal volumes of methyl-tert-butyl ether (MTBE) and KOH:methanol mixture (1:9, w/v) overnight in the dark and mixed with 2 ml of MTBE and 2 ml of distilled water. The supernatant was dried and dissolved in MTBE containing 0.1% butylated hydroxytoluene. Samples were automatically loaded into the reverse-phase HPLC system and analyzed with Agilent ChemStation software. β-Carotene (C4582, Sigma-Aldrich) was quantified using an external standard.

RNAi

Double-stranded RNAs (dsRNAs) were synthesized by in vitro transcription with the T7 RiboMAX Express RNAi System (Promega, USA) following the manufacturer′s instructions. dsRNA concentrations were determined with an ND-1000 spectrophotometer, and dsRNA quality was verified through 1% agarose gel electrophoresis. Three micrograms of dsRNA was injected into the second ventral segment of the abdomen at day 2 for the second- or third-instar nymphs three or four times over 48-hour intervals. After two stadia, the effects of RNAi were determined through qRT-PCR.

Electroporation-mediated RNAi was conducted according to a previous study (*49*). Nymphs were anesthetized and covered with wet paper on ice for 3 min. Then, 2 μl of 100 μM dsRNA solution was injected into the intersegmental membrane between the hind leg and metathorax for RNAi in the thorax. Following the injection of the dsRNA solution, two droplets of LOGIQLEAN Gel for Ultrasound Hard type (GE Healthcare) were applied to the nymphal surface. The electrode (1 mmϕ) was placed on the ultrasound gel, with a positive electrode on the side injected with the dsRNA solution and a negative electrode on the opposite side. Ten electroporation pulses (280 ms/s each, 45 V) were generated using the Curegene electroporator (CellProduce). The treated nymphs were returned to gregarious rearing cages (Perspex boxes, 15 cm by 15 cm by 11 cm). After nymphal ecdysis, the phenotype around the region where the positive electrode was placed for electroporation was observed and photographed using a stereoscopic microscope S8APO (Leica Microsystems).

Scanning electron microscopy

Nymphal integuments fixed with 2.5% glutaraldehyde in 0.1 M PBS were dried in vacuo. The samples were gold-coated via a Smart Coater (JEOL) and observed under a scanning electron microscope (JCM 6000, JEOL).

Immunohistochemical analysis

The integuments were dissected and fixed in 4% paraformaldehyde at 4°C overnight. Paraffin-embedded integument tissue sections (7 μm thick) were deparaffinized and rehydrated. The sections were blocked with 5% BSA for 1 hour and incubated with anti-βCBP antibodies (1:200), anti-ATF2 antibodies (1:500), or anti–pS-ATF2 (1:500) for the primary antibodies at 4°C overnight. After being washed with 0.1 M PBS, the slides were blocked with 3% BSA for 30 min and then incubated with Alexa Fluor 488 (green) or Alexa Fluor 594 (red) goat anti-rabbit IgG as a secondary antibody (Life Technologies) at 37°C for 1 hour. The nuclei were labeled with 4′,6-diamidino-2-phenylindole (1:1000). Fluorescence was detected under an LSM 710 confocal laser-scanning microscope (Zeiss).

TF prediction of the β*CBP* promoter

The promoter sequence of β*CBP* was amplified by using the Genome Walking Kit (TaKaRa) following the manufacturer′s protocol based on the known upstream sequence of β*CBP* obtained from the *L. migratoria* genome in our laboratory. The obtained upstream genome sequence of β*CBP* was used to predict the potential CREs and putative TFs via the TANSFAC program (http://genexplain.com/transfac/).

Luciferase reporter assay

The upstream regions of β*CBP* with different lengths were amplified from *L. migratoria* genomic DNA and subcloned into the pGL4.1 vector fused with a firefly luciferase marker gene (Promega). The coding sequences of putative TFs were cloned into the pAc5.1/V5-His b (pAc5.1b) expression vector (Invitrogen) for expression in S2 cells. Mutants of ATF2-M1 (amino acids 6 to 186 deleted), ATF2-M2 (amino acids 268 to 382 deleted) and ATF2-M3 (amino acids 457 to 577 deleted) were cloned into the pAc5.1b expression vector to validate the binding of the TF domain to the regulatory element. A mutated serine site of ATF2 (S45A, S327A, S406A, S518A, and S668A) expression vector was generated to validate the active phosphorylation site of ATF2. The primers used for the construction of recombinant plasmids are listed in table S4.

S2 cells were cultured at 28°C in a 24-well plate 6 hours before transfection. The pGL4.1-derived constructs and a reference reporter pGL4.73 vector (Promega) containing a *Renilla* luciferase gene were separately transfected or cotransfected with pAc5.1b-TFs into S2 cells for 48 hours at 28°C using Lipofectamine 3000 (Invitrogen, CA, USA). The transfected cells were incubated with PKC inhibitor (Gö6976, Selleck), ERK inhibitor (PD98059, Cell Signaling Technology), p38 inhibitor (SB202190, Cell Signaling Technology), or JNK inhibitor (SP600125, Cell Signaling Technology) for luciferase reporter assays with inhibitors. Luciferase activity was determined using the Dual-Luciferase Reporter Assay System with a GloMax 96 Microplate Luminometer (Promega) according to the manufacturer′s instructions. The luciferase activity was defined as the ratio of firefly luciferase activity to *Renilla* luciferase activity.

Electrophoretic mobility shift assay

An EMSA was performed using the Light Shift Chemiluminescent EMSA Kit (Thermo Fisher Scientific, Waltham, USA) according to the manufacturer′s protocols. The oligonucleotide probes labeled with biotin at the 5′ end were synthesized by Invitrogen Company (Shanghai, China) and annealed to generate the double-stranded probe by natural cooling. The oligonucleotide probes used in this study are listed in table S5.

Nuclear proteins were extracted from S2 cells overexpressing ATF2 using a nuclear extract kit (R0050, Solarbio, Shanghai, China). One microgram of extracted protein was incubated with 0.25 μM biotin-labeled probes in a 20 μl of mixture buffer containing 2.5% glycerol, 0.05% NP-40, 50 mM KCl, 5 mM $MgCl_2$, 4 mM EDTA, and 50 ng of poly(deoxyinosinic-deoxycytidylic) at room temperature for 20 min. Cold probes (unbiotinylated) were added to the binding reaction for the competition assay. One microgram of His antibody or rabbit IgG was added to the binding reaction for the super shift assay. The samples were then separated using a 6% polyacrylamide gel and blotted onto a nylon membrane. The membrane was exposed to ultraviolet light crosslinking for 300 s and then incubated with a streptavidin–horseradish peroxidase (HRP) conjugate. The DNA in the gel was detected by a chemiluminescent nucleic acid detection module (Thermo Fisher Scientific) via a 5200 Chemiluminescence Imaging System (Tanon Science & Technology, Shanghai, China).

Western blotting

Protein from integuments was extracted in ice-cold lysis buffer [150 mM NaCl, 0.5% NP-40, 0.5% sodium deoxycholate, and 50 mM (pH 7.4) tris-HCl] with protease and phosphatase inhibitor mixtures (Roche). Protein samples were fractionated using 12% SDS-PAGE and transferred onto a nitrocellulose membrane (Merck Millipore). In addition, Phos-tag SDS-PAGE gel was prepared by adding an additional 100 μM $MnCl_2$ and 50 μM Phos-tag (Wako, Japan) to the 12% SDS-PAGE. Phos-tag SDS-PAGE gels were washed twice by gently shaking in transfer buffer containing 10 mM EDTA for 10 min and incubated in transfer buffer without EDTA for 10 min before being transferred to polyvinylidene fluoride membranes (Merck Millipore). After blocking with 3% BSA, the membrane was incubated with the corresponding primary antibodies and subsequently with HRP-conjugated secondary antibodies (Proteintech) and visualized using the chemiluminescent nucleic acid detection module (Thermo Fisher Scientific). The blotting band intensity was determined using ImageJ software (NIH, Bethesda, MD, USA). It should be noted that Phos-tag SDS-PAGE can detect phosphorylated and nonphosphorylated proteins by their band shift differences.

λPPase treatment

The protein was extracted from the integuments via lysis buffer. After centrifugation at 10,000*g* at 4°C for 10 min, 40 μl of the supernatant was incubated with 0.5 μl of λPPase, 5 μl of buffer, and 5 μl of $MnCl_2$ at 30°C for 30 min according to the manufacturer′s specifications (New England Biolabs) and then was subjected to Western blotting analysis.

Extraction of nuclear and cytoplasmic proteins

Nuclear and cytoplasmic proteins were extracted from the pronotum and the prosternum of gregarious locust nymphs using a nuclear and cytoplasmic extraction kit (Beyotime, Jiangsu, China) according to the manufacturer′s specifications. The cytoplasmic and nuclear protein extracts were used for Western blotting analysis. The reference proteins for nuclear and cytoplasmic proteins were detected with polyclonal anti-H3 antibody and anti–β-actin antibody, respectively.

ATF2 protein isolation

Anti-ATF2 polyclonal antibodies were conjugated with cyanogen bromide (CNBr)–activated Sepharose 4B according to the manufacturer′s instructions (GE Healthcare). Proteins were extracted using lysis buffer with protease and phosphatase inhibitor mixtures (Roche), and 40 μl of supernatant was used as the protein input. The remaining supernatant was added to the treated column and incubated at 4°C overnight with gentle shaking. After the column was washed with tris-buffered saline buffer [0.1 M tris-HCl and 0.5 M NaCl (pH 8.0)], protein was eluted with 200 μl of 0.1 M glycine (pH 2.5) and 10 μl of 1 M tris-HCl (pH 8.0). The eluted proteins were then assessed with SDS-PAGE for Western blotting analysis.

Coimmunoprecipitation

Total proteins were extracted from integuments using lysis buffer supplemented with protease and phosphatase inhibitor mixtures (Roche). Approximately 10% of the total protein was reserved as input before the lysate was centrifuged at 12,000*g* for 10 min at 4°C. The remaining supernatant was incubated with 1 μg of anti-ATF2 antibodies with gentle agitation overnight at 4°C. IgG antibody was used as a negative control. Ten microliters of protein A beads (Thermo Fisher Scientific) was added to capture the antibodies for 1 hour with agitation at 4°C. The beads were washed five times with immunoprecipitation buffer. The immunoprecipitates with beads were boiled in 1% SDS-PAGE loading buffer and then subjected to SDS-PAGE and Western blotting.

Phosphorylation site prediction and identification

Phosphorylation sites and the corresponding kinases were predicted by NetPhos 3.1 software (https://services.healthtech.dtu.dk/service.php?NetPhos-3.1). The isolated ATF2 proteins extracted from G-Pros were subjected to 12% SDS-PAGE and stained with Coomassie brilliant blue R-250. The gels were destained with destaining solution (10% acetic acid, 5% ethanol, and 85% water), and the differentiated protein bands were excised for identification of ATF2 phosphorylation modifications via LC-MS/MS analysis (PTM Biolabs, Hangzhou, China).

Bioinformatic analysis and phylogenetic analysis

The protein sequences of *Drosophila* TFs were used to search for their homologs in the locust genome and transcriptome database by using the tblastn algorithm. Protein structural domains were analyzed using Simple Modular Architecture Research Tool (http://smart.embl-heidelberg.de/), and multiple sequence alignments were generated via DNAMAN software (Lynnon Biosoft, San Ramon, CA, USA). Molecular phylogenetic analyses were conducted by the neighbor-joining method using Molecular Evolutionary Genetics Analysis 7, and the number of bootstrap replications was 1000.

Chromatin immunoprecipitation

ChIP assays were performed using the Pierce Agarose ChIP Kit (Thermo Fisher Scientific) in accordance with the manufacturer's instructions. The integuments from nymphs were crushed and fixed with 1% formaldehyde to crosslink chromatin for 10 min at 37°C before being incubated with 125 mM glycine. After the addition of lysis buffer [50 mM Hepes (pH 7.5), 140 mM NaCl, 1% Triton X-100, protease, and phosphatase inhibitors], the chromatin was sonicated to shear into 200- to 1000-bp DNA fragments. After centrifugation, the supernatant was diluted with dilution buffer [16.7 mM tris-HCl (pH 8.1), 167 mM NaCl, 0.01% SDS, and 1.1% Triton X-100]. The complexes were then immunoprecipitated with antibodies against ATF2, pS-ATF2, or normal rabbit IgG (Cell Signaling Technology) at 4°C overnight, followed by incubation with ChIP Grade Protein A/G Plus Agarose at 4°C for 2 hours. After the beads were sequentially washed with low-salt buffer three times, high-salt buffer three times, and tris-EDTA (TE) buffer two times, the DNA was eluted in elution buffer (1% SDS and 0.1 M $NaHCO_3$). After ribonuclease and Protease K treatment, the DNA was purified using spin columns following the manufacturer's instructions and used as the template for qRT-PCR. The primers used for ChIP are listed in table S3. Antibodies against ATF2 and IgG were used as the positive and negative controls, respectively.

Statistical analyses

All data are shown as the means ± SDs of at least three biologically independent experiments. The statistical significance of differences between samples was analyzed using Student's *t* test for the comparison ($^{*}P < 0.05$, $^{**}P < 0.01$, $^{***}P < 0.001$, and $^{****}P < 0.0001$) or one-way analysis of variance (ANOVA) for multiple comparisons using Tukey's multiple comparison test and a $P = 0.05$ significance threshold level (GraphPad Prism 8, San Diego, CA).

Supplementary Materials

This PDF file includes:
Figs. S1 to S11
Legend for table S1
Tables S2 to S5
References

Other Supplementary Material for this manuscript includes the following:
Table S1

REFERENCES AND NOTES

1. R. V. Alatalo, J. Mappes, Tracking the evolution of warning signals. *Nature* **382**, 708–710 (1996).
2. J. L. Gittleman, P. H. Harvey, Why are distasteful prey not cryptic. *Nature* **286**, 149–150 (1980).
3. K. L. Prudic, J. C. Oliver, F. A. H. Sperling, The signal environment is more important than diet or chemical specialization in the evolution of warning coloration. *Proc. Natl. Acad. Sci. U.S.A.* **104**, 19381–19386 (2007).
4. H. B. Cott, *Adaptive Coloration in Animals* (Methuen and Co. Ltd., 1940).
5. M. P. Pener, S. J. Simpson, Locust phase polyphenism: An update. *Adv. Insect Physiol.* **36**, 1–272 (2009).
6. M. P. Pener, Locust phase polymorphism and its endocrine relations. *Adv. Insect Physiol.* **23**, 1–79 (1991).
7. X. Wang, L. Kang, Molecular mechanisms of phase change in locusts. *Annu. Rev. Entomol.* **59**, 225–244 (2014).
8. S. Tanaka, K. I. Harano, Y. Nishide, R. Sugahara, The mechanism controlling phenotypic plasticity of body color in the desert locust: Some recent progress. *Curr. Opin. Insect Sci.* **17**, 10–15 (2016).
9. S. Clusella Trullas, J. H. van Wyk, J. R. Spotila, Thermal melanism in ectotherms. *J. Therm. Biol.* **32**, 235–245 (2007).
10. J. N. Wei, W. B. Shao, M. M. Cao, J. Ge, P. C. Yang, L. Chen, X. H. Wang, L. Kang, Phenylacetonitrile in locusts facilitates an antipredator defense by acting as an olfactory aposematic signal and cyanide precursor. *Sci. Adv.* **5**, eaav5495 (2019).
11. J. Vetter, Plant cyanogenic glycosides. *Toxicon* **38**, 11–36 (2000).
12. L. P. Brower, S. C. Glazier, Localization of heart poisons in the monarch butterfly. *Science* **188**, 19–25 (1975).
13. S. W. Applebaum, E. Avisar, Y. Heifetz, Juvenile hormone and locust phase. *Arch. Insect Biochem.* **35**, 375–391 (1997).
14. M. L. Yang, Y. L. Wang, Q. Liu, Z. K. Liu, F. Jiang, H. M. Wang, X. J. Guo, J. Z. Zhang, L. Kang, A β-carotene-binding protein carrying a red pigment regulates body-color transition between green and black in locusts. *eLife* **8**, e41362 (2019).
15. S. Yoda, K. Sakakura, T. Kitamura, Y. Kondo, K. Sato, R. Ohnuki, I. Someya, S. Komata, T. Kojima, S. Yoshioka, H. Fujiwara, Genetic switch in UV response of mimicry-related pale-yellow colors in Batesian mimic butterfly, *Papilio polytes*. *Sci. Adv.* **7**, eabd6475 (2021).
16. N. J. Nadeau, C. Pardo-Diaz, A. Whibley, M. A. Supple, S. V. Saenko, R. W. Wallbank, G. C. Wu, L. Maroja, L. Ferguson, J. J. Hanly, H. Hines, C. Salazar, R. M. Merrill, A. J. Dowling, R. H. ffrench-Constant, V. Llaurens, M. Joron, W. O. McMillan, C. D. Jiggins, The gene *cortex* controls mimicry and crypsis in butterflies and moths. *Nature* **534**, 106–110 (2016).
17. Y. Tomoyasu, Y. Arakane, K. J. Kramer, R. E. Denell, Repeated co-options of exoskeleton formation during wing-to-elytron evolution in beetles. *Curr. Biol.* **19**, 2057–2065 (2009).
18. M. Gautier, J. Yamaguchi, J. Foucaud, A. Loiseau, A. Ausset, B. Facon, B. Gschloessl, J. Lagnel, E. Loire, H. Parrinello, D. Severac, C. Lopez-Roques, C. Donnadieu, M. Manno, H. Berges, K. Gharbi, L. Lawson-Handley, L. S. Zang, H. Vogel, A. Estoup, B. Prud'homme, The genomic basis of color pattern polymorphism in the harlequin ladybird. *Curr. Biol.* **28**, 3296–3302 (2018).
19. E. Reszczynska, R. Welc, W. Grudzinski, K. Trebacz, W. I. Gruszecki, Carotenoid binding to proteins: Modeling pigment transport to lipid membranes. *Arch. Biochem. Biophys.* **584**, 125–133 (2015).
20. X. H. Wang, X. D. Fang, P. C. Yang, X. T. Jiang, F. Jiang, D. J. Zhao, B. L. Li, F. Cui, J. N. Wei, C. A. Ma, Y. D. Wang, J. He, Y. Luo, Z. F. Wang, X. J. Guo, W. Guo, X. S. Wang, Y. Zhang, M. L. Yang, S. G. Hao, B. Chen, Z. Y. Ma, D. Yu, Z. Q. Xiong, Y. B. Zhu, D. D. Fan, L. J. Han, B. Wang, Y. X. Chen, J. W. Wang, L. Yang, W. Zhao, Y. Feng, G. X. Chen, J. M. Lian, Q. Y. Li, Z. Y. Huang, X. M. Yao, N. Lv, G. J. Zhang, Y. R. Li, J. Wang, J. Wang, B. L. Zhu, L. Kang, The locust genome provides insight into swarm formation and long-distance flight. *Nat. Commun.* **5**, 2957 (2014).
21. K. Cartharius, K. Frech, K. Grote, B. Klocke, M. Haltmeier, A. Klingenhoff, M. Frisch, M. Bayerlein, T. Werner, MatInspector and beyond: Promoter analysis based on transcription factor binding sites. *Bioinformatics* **21**, 2933–2942 (2005).
22. E. Wingender, P. Dietze, H. Karas, R. Knuppel, TRANSFAC: A database on transcription factors and their DNA binding sites. *Nucleic Acids Res.* **24**, 238–241 (1996).
23. T. Yamasaki, A. Takahashi, J. Z. Pan, N. Yamaguchi, K. K. Yokoyama, Phosphorylation of activation transcription factor-2 at serine 121 by protein kinase C controls c-Jun-mediated activation of transcription. *J. Biol. Chem.* **284**, 8567–8581 (2009).
24. E. Lau, H. Kluger, T. Varsano, K. Lee, I. Scheffler, D. L. Rimm, T. Ideker, Z. A. Ronai, PKCε promotes oncogenic functions of ATF2 in the nucleus while blocking its apoptotic function at mitochondria. *Cell* **148**, 543–555 (2012).
25. S. Gupta, D. Campbell, B. Derijard, R. J. Davis, Transcription factor ATF2 regulation by the JNK signal transduction pathway. *Science* **267**, 389–393 (1995).
26. D. M. Ouwens, N. D. de Ruiter, G. C. M. van der Zon, A. P. Carter, J. Schouten, C. van der Burgt, K. Kooistra, J. L. Bos, J. A. Maassen, H. van Dam, Growth factors can activate ATF2 via a two-step mechanism: Phosphorylation of Thr71 through the Ras-MEK-ERK pathway and of Thr69 through RalGDS-Src-p38. *EMBO J.* **21**, 3782–3793 (2002).
27. E. J. Denton, Review lecture: On the organization of reflecting surfaces in some marine animals. *Philos. Trans. R. Soc. Lond. B Biol. Sci.* **258**, 285–313 (1970).
28. W. L. Allen, R. Baddeley, I. C. Cuthill, N. E. Scott-Samuel, A quantitative test of the predicted relationship between countershading and lighting environment. *Am. Nat.* **180**, 762–776 (2012).
29. M. Stevens, S. Merilaita, *Animal camouflage : Mechanisms and function* (Cambridge Univ. Press, 2012), pp. xii, pp. 357–316 of col. plates.
30. G. A. Sword, Density-dependent warning coloration. *Nature* **397**, 217 (1999).
31. J. Skelhorn, C. G. Halpin, C. Rowe, Learning about aposematic prey. *Behav. Ecol.* **27**, 955–964 (2016).
32. R. H. J. Brown, Mechanism of locust jumping. *Nature* **214**, 939 (1967).

33. R. D. Santer, Y. Yamawaki, F. C. Rind, P. J. Simmons, Motor activity and trajectory control during escape jumping in the locust *Locusta migratoria*. *J. Comp. Physiol. A* **191**, 965–975 (2005).
34. J. B. Barnett, C. Michalis, N. E. Scott-Samuel, I. C. Cuthill, Distance-dependent defensive coloration in the poison frog *Dendrobates tinctorius,* Dendrobatidae. *Proc. Natl. Acad. Sci. U.S.A.* **115**, 6416–6421 (2018).
35. N. Howell, C. Sheard, M. Koneru, K. Brockelsby, K. Ono, T. Caro, Aposematism in mammals. *Evolution* **75**, 2480–2493 (2021).
36. M. E. Maan, M. E. Cummings, Poison frog colors are honest signals of toxicity, particularly for bird predators. *Am. Nat.* **179**, E1–14 (2012).
37. H. Chang, S. Cassau, J. Krieger, X. Guo, M. Knaden, L. Kang, B. S. Hansson, A chemical defense deters cannibalism in migratory locusts. *Science* **380**, 537–543 (2023).
38. D. A. Cullen, G. A. Sword, G. G. Rosenthal, S. J. Simpson, E. Dekempeneer, M. Hertog, B. M. Nicolai, R. Caes, L. Mannaerts, J. Vanden Broeck, Sexual repurposing of juvenile aposematism in locusts. *Proc. Natl. Acad. Sci. U.S.A.* **119**, e2200759119 (2022).
39. I. C. Cuthill, W. L. Allen, K. Arbuckle, B. Caspers, G. Chaplin, M. E. Hauber, G. E. Hill, N. G. Jablonski, C. D. Jiggins, A. Kelber, J. Mappes, J. Marshall, R. Merrill, D. Osorio, R. Prum, N. W. Roberts, A. Roulin, H. M. Rowland, T. N. Sherratt, J. Skelhorn, M. P. Speed, M. Stevens, M. C. Stoddard, D. Stuart-Fox, L. Talas, E. Tibbetts, T. Caro, The biology of color. *Science* **357**, eaan0221 (2017).
40. I. Bleichman, P. Yadav, A. Ayali, Visual processing and collective motion-related decision-making in desert locusts. *Proc. R. Soc. B* **290**, 20221862 (2023).
41. P. Lopez-Bergami, E. Lau, Z. Ronai, Emerging roles of ATF2 and the dynamic AP1 network in cancer. *Nat. Rev. Cancer* **10**, 65–76 (2010).
42. K. R. L. van der Burg, J. J. Lewis, B. J. Brack, R. A. Fandino, A. Mazo-Vargas, R. D. Reed, Genomic architecture of a genetically assimilated seasonal color pattern. *Science* **370**, 721–725 (2020).
43. S. Wang, D. Teng, X. Li, P. Yang, W. Da, Y. Zhang, Y. Zhang, G. Liu, X. Zhang, W. Wan, Z. Dong, D. Wang, S. Huang, Z. Jiang, Q. Wang, D. J. Lohman, Y. Wu, L. Zhang, F. Jia, E. Westerman, L. Zhang, W. Wang, W. Zhang, The evolution and diversification of oakleaf butterflies. *Cell* **185**, 3138–3152 (2022).
44. Y. Kondo, S. Yoda, T. Mizoguchi, T. Ando, J. Yamaguchi, K. Yamamoto, Y. Banno, H. Fujiwara, Toll ligand Spätzle3 controls melanization in the stripe pattern formation in caterpillars. *Proc. Natl. Acad. Sci. U.S.A.* **114**, 8336–8341 (2017).
45. A. Bhoumik, S. Takahashi, W. Breitweiser, Y. Shiloh, N. Jones, Z. Ronai, ATM-dependent phosphorylation of ATF2 is required for the DNA damage response. *Mol. Cell* **18**, 577–587 (2005).
46. J. Raingeaud, S. Gupta, J. S. Rogers, M. Dickens, J. H. Han, R. J. Ulevitch, R. J. Davis, Pro-inflammatory cytokines and environmental-stress cause p38 mitogen-activated protein-kinase activation by dual phosphorylation on Tyrosine and Threonine. *J. Biol. Chem.* **270**, 7420–7426 (1995).
47. B. Baan, H. van Dam, G. C. van der Zon, J. A. Maassen, D. M. Ouwens, The role of c-Jun N-terminal kinase, p38, and extracellular signal-regulated kinase in insulin-induced Thr69 and Thr71 phosphorylation of activating transcription factor 2. *Mol. Endocrinol.* **20**, 1786–1795 (2006).
48. H. Y. Park, J. Lee, S. Gonzalez, M. A. Middelkamp-Hup, S. Kapasi, S. Peterson, B. A. Gilchrest, Topical application of a protein kinase C inhibitor reduces skin and hair pigmentation. *J. Invest. Dermatol.* **122**, 159–166 (2004).
49. H. Jin, T. Seki, J. Yamaguchi, H. Fujiwara, Prepatterning of *Papilio xuthus* caterpillar camouflage is controlled by three homeobox genes: *clawless*, *abdominal-A*, and *Abdominal-B*. *Sci. Adv.* **5**, eaav7569 (2019).
50. Y. Perez-Riverol, J. Bai, C. Bandla, D. Garcia-Seisdedos, S. Hewapathirana, S. Kamatchinathan, D. J. Kundu, A. Prakash, A. Frericks-Zipper, M. Eisenacher, M. Walzer, S. Wang, A. Brazma, J. A. Vizcaino, The PRIDE database resources in 2022: A hub for mass spectrometry-based proteomics evidences. *Nucleic Acids Res.* **50**, 543–552 (2022).
51. M. Zhang, X. Chen, J. Zhang, B. Guo, J. Li, Z. Bai, Analysis of protein kinase C (*HcPKC*) gene expression and single-nucleotide polymorphisms related to inner shell color traits in *Hyriopsis cumingii*. *BMC Genom. Data* **23**, 71 (2022).
52. N. I. Mundy, J. Stapley, C. Bennison, R. Tucker, H. Twyman, K. W. Kim, T. Burke, T. R. Birkhead, S. Andersson, J. Slate, Red carotenoid coloration in the zebra finch is controlled by a cytochrome P450 gene cluster. *Curr. Biol.* **26**, 1435–1440 (2016).
53. M. B. Toomey, C. I. Marques, P. M. Araujo, D. Huang, S. Zhong, Y. Liu, G. D. Schreiner, C. A. Myers, P. Pereira, S. Afonso, P. Andrade, M. A. Gazda, R. J. Lopes, I. Viegas, R. E. Koch, M. E. Haynes, D. J. Smith, Y. Ogawa, D. Murphy, R. E. Kopec, D. M. Parichy, M. Carneiro, J. C. Corbo, A mechanism for red coloration in vertebrates. *Curr. Biol.* **32**, 4201–4214 (2022).
54. Y. C. Wei, X. Li, D. Q. Zhang, Y. F. Liu, Comparison of protein differences between high- and low-quality goat and bovine parts based on iTRAQ technology. *Food Chem.* **289**, 240–249 (2019).
55. L. Qian, S. Qi, F. Cao, J. Zhang, C. Li, M. Song, C. Wang, Effects of penthiopyrad on the development and behaviour of zebrafish in early-life stages. *Chemosphere* **214**, 184–194 (2019).
56. M. B. Toomey, R. J. Lopes, P. M. Araujo, J. D. Johnson, M. A. Gazda, S. Afonso, P. G. Mota, R. E. Koch, G. E. Hill, J. C. Corbo, M. Carneiro, High-density lipoprotein receptor SCARB1 is required for carotenoid coloration in birds. *Proc. Natl. Acad. Sci. U.S.A.* **114**, 5219–5224 (2017).
57. J. D. Johnson, G. E. Hill, Is carotenoid ornamentation linked to the inner mitochondria membrane potential? A hypothesis for the maintenance of signal honesty. *Biochimie* **95**, 436–444 (2013).
58. M. Seyfert, R. A. Mancini, M. C. Hunt, J. Tang, C. Faustman, M. Garcia, Color stability, reducing activity, and cytochrome c oxidase activity of five bovine muscles. *J. Agric. Food Chem.* **54**, 8919–8925 (2006).
59. E. Marchal, J. Zhang, L. Badisco, H. Verlinden, E. F. Hult, P. Van Wielendaele, K. J. Yagi, S. S. Tobe, J. Vanden Broeck, Final steps in juvenile hormone biosynthesis in the desert locust, *Schistocerca gregaria*. *Insect Biochem. Mol. Biol.* **41**, 219–227 (2011).
60. M. R. Lakshman, C. Okoh, Carotenoid-protein complexes. *Method. Enzymol.* **214**, 74–86 (1993).

Acknowledgments: We thank L. Hou from the State Key Laboratory of Integrated Management of Pest Insects and Rodents, Institute of Zoology, Chinese Academy of Sciences, China for the invaluable comments on this study. **Funding:** The research was supported by grants from the Natural Science Foundation of China (NSFC) (grant nos. 32088102, 31920103004, 32070505, 31872302, and 31872303), the National Key Research and Development Program of China (grant no. 2022YFD1400503), the China National Postdoctoral Program for Innovation Talents (grant no. BX2021304), the Beijing Natural Science Foundation (grant no. 6224063), the Support Project of High level Teachers in Beijing Municipal Universities in the Period of 14th Five–year Plan (grant no. BPHR20220114), and the China Postdoctoral Science Foundation (grant no. 2020 M680669). **Author contributions:** Conceptualization: X.K., M.Y., and L.K. Methodology: X.K., M.Y., X.C., and H.W. Investigation: X.K., M.Y., X.C., and H.W. Supervision: M.Y. and L.K. Writing—original draft: X.K. Writing—review and editing: X.K., M.Y., and L.K. **Competing interests:** The authors declare that they have no competing interests. **Data and materials availability:** All data needed to evaluate the conclusions in the paper are present in the paper and/or the Supplementary Materials. The MS proteomics data have been deposited to the ProteomeXchange Consortium via the PRIDE (*50*) partner repository with the dataset identifier PXD042860.

Submitted 2 May 2023
Accepted 22 July 2023
Published 23 August 2023
10.1126/sciadv.adi5168